

# Model sensitivity across scales: a case study of simulating an offshore low-level jet

Patrick Hawbecker<sup>1</sup>, William Lassman<sup>2</sup>, Timothy W. Juliano<sup>1</sup>, Branko Kosović<sup>3</sup>, and Sue Ellen Haupt<sup>1</sup>

<sup>1</sup>National Center for Atmospheric Research; 3450 Mitchell Ln, Boulder, CO 80301, USA

<sup>2</sup>Xcel Energy; work performed while at Lawrence Livermore National Laboratory, Livermore, CA 94550, USA

<sup>3</sup>Johns Hopkins University, Baltimore, MD 21218, USA

**Correspondence:** Patrick Hawbecker (hawbecker@ucar.edu)

**Abstract.** In this study, a seven-member ensemble of mesoscale-to-microscale simulations with varying sea surface temperature (SST) is conducted for a case in which an offshore low-level jet was observed via floating lidar. The performance of each SST setup in reproducing physical characteristics of the observed low-level jet is compared across the mesoscale and microscale domains. It is shown that the representation of low-level shear, jet nose height, and hub-height wind speed are **generally** improved when moving from mesoscale to microscale. Specifically, low-level shear is improved in the microscale by reducing near-surface wind speeds and lowering the jet nose height to be closer to that observed. Counterintuitively, the sensible heat flux on the mesoscale domains is more negative than on the microscale domains, which would indicate a more stable boundary layer with higher shear; however, the low-level shear in the mesoscale is weaker than that of the microscale domains. This indicates over-mixing of the PBL **scheme** in the mesoscale domains and/or over-prediction of surface drag in the microscale domain.

We analyze performance considering a real-world scenario in which the computational burden of running an ensemble of LES limits a study to performing a mesoscale ensemble to select the *best* model setup that will drive a single LES run. In the context of this study, the best model setup is subjective and weighs model performance in the physical representation of the low-level jet as well as the model surface forcing through the temperature gradient between air and sea. The expectation of this approach is that the best performing setup of the mesoscale simulations will produce the best result for the microscale simulations. It is shown that there are large fundamental changes in the characteristics of the low-level jet as well as in the surface forcing conditions between the mesoscale and microscale domains. This results in a non-linear ranking of performance between the mesoscale domains and the microscale domains. While the best performing mesoscale setup is also deemed to produce the best results on the microscale, the second best performing mesoscale setup produces the worst results on the microscale.

## 1 Introduction

Conducting large-eddy simulations (LES) driven by mesoscale numerical weather prediction (NWP) models for real data cases has become increasingly popular for meteorological and wind energy related studies. With advances in computational power, it is increasingly manageable to run LES on large domains (e.g., tens of kilometers) down to fine scales (e.g., several meters) in

25 order to simulate complex flows and atmospheric phenomena of interest. However, studies running simulations in this manner  
are often limited to a single LES run due to the computational burden. In real data cases, domain sizes often are quite large  
while model grid spacing,  $\Delta_x$ , is in the 10's of meters if not smaller. LES domains must be sufficiently large in size in order  
to capture the meteorological event of interest. Additionally, periodicity is not an appropriate boundary condition for real data  
30 conditions for the LES are typically derived from NWP models at mesoscale resolution. When nesting down to LES scales the  
model is tasked with filling in the energy, or turbulence, at scales not resolved by the mesoscale model at the boundaries. This  
requires time and distance for turbulence to develop known as “fetch” (Muñoz-Esparza et al., 2014; Mirocha et al., 2014; Haupt  
et al., 2019, 2020). While there are techniques to decrease the turbulent fetch region, such as the stochastic cell perturbation  
technique used in this study (Muñoz-Esparza et al., 2014, 2015), they still require a considerable amount of the domain to  
35 be dedicated strictly to developing adequate turbulence. From this, boundary-coupled mesoscale-to-LES simulations often  
demand a large domain size for the LES while retaining a small grid spacing. The LES domain will also require time to spin-up  
turbulence before the flow field can be analyzed. Thus, running such simulations is often computationally expensive.

For case studies in which obtaining an accurate representation of the flow field at turbulence-resolving scales from LES is  
required, minimizing computational cost can be challenging. One approach is to run several mesoscale simulations (which are  
40 relatively inexpensive, computationally) to find the best performing *mesoscale* setup and then use that setup to drive the LES.  
The assumption in this approach is that the domain-averaged LES solution will not differ largely from the mesoscale result,  
and that the sensitivity on the mesoscale will directly translate to the microscale. Thus, the best performing mesoscale setup is  
presumed to lead to the best performing microscale setup.

In this study, model sensitivity of an offshore low-level jet (LLJ) to sea-surface temperature (SST) is analyzed across both  
45 the mesoscale and microscale. The goal is to assess [the , on both the mesoscale and microscale, the](#) sensitivity of LLJ char-  
acteristics [and to SST and model](#) performance when compared to observations in order to determine whether the assumptions  
above are indeed valid.

The parameter choices for this sensitivity study are twofold. First, model results are likely sensitive to many factors such  
as turbulence closure, surface layer parameterization, initial and boundary conditions, etc. When adjusting parameterizations  
50 such as the planetary boundary layer (PBL) scheme on the mesoscale domain, there is no direct corollary for these PBL  
schemes on the microscale. In Talbot et al. (2012), sensitivity to the PBL scheme was assessed on the mesoscale domain along  
with the sub-grid scale turbulence closure scheme on the microscale domain. While the PBL scheme and sub-grid turbulence  
closure schemes have similar functions, they are not directly comparable across scales. Thus, it is difficult to assess how model  
sensitivity changes across scales when the mesoscale and microscale domains are each run with varying turbulence closure  
55 techniques. Additionally, other parameterizations within the model are scale-sensitive and their impacts vary as  $\Delta_x$  changes.  
[Thus, it is important to select](#) [This highlights the importance of selecting](#) a parameter that will impact the mesoscale and microscale  
domains similarly to assess how sensitivity changes across scales.

A second consideration for parameter choice is to provide a way to vary the characteristics of the LLJ. [Offshore low-  
level jets can form when relatively warmer air advects over colder water temperatures generating stable conditions and](#)

60 frictional decoupling of the winds aloft (see De Jong et al. (2024) for more information on offshore low-level jet formation mechanisms in this region). As offshore wind energy continues to grow in the United States, observations have shown that LLJs are a common occurrence off the coast of the Mid-Atlantic and Northeast states (Zhang et al., 2006; Colle and Novak, 2010; Nunalee and Basu, 2014; Colle et al., 2016; Pichugina et al., 2017; Strobach et al., 2018; Debnath et al., 2021) (Zhang et al., 2006; Colle and Novak, 2010; Nunalee and Basu, 2014; Colle et al., 2016; Pichugina et al., 2017; Strobach et al., 2018; Debnath et al., 2021; Aird et al., 2022; De Jong et al., 2024; Quint et al., 2025) and their impacts on energy production and turbine performance must be considered (McCabe and Freedman, 2025; Paulsen et al., 2025). These LLJs have been shown to have jet noses frequently below 100 m, which would mean in the offshore environment, where turbines are larger than those on land, the shear profile across the rotor could be very complex. The presence of negative shear over the rotor swept area is shown to impact turbine loads and stresses and decrease wake recovery (Wharton and Lundquist, 2012; Bhaganagar and Debnath, 2014; Park et al., 2014; Gutierrez et al., 2017; Kalverla et al., 2019; Gadde and Stevens, 2021). Debnath et al. (2021) showed relationships between the temperature difference ( $\Delta T$ ) between air (2 m 2-m temperature) and sea (SST) and the occurrence and strength of strong shear or LLJ events in the New York Bight. Thus, any changes in  $\Delta T$  are likely to augment the characteristics of the LLJ. We elect to vary SST in this study as a simple way to augment  $\Delta T$  that is consistent across all domains.

75 Preliminary results of this study have been presented (Hawbecker et al., 2022) and a brief summary of the project and high-level conclusions have been shared in Haupt et al. (2023). Here, we share in more detail the full analysis of this study as well as additional conclusions pertaining to the differences in mesoscale and LES performance, surface characteristics and their impact of the simulated LLJ, and important requirements for running WRF at high resolution (O(1-10)m). Figures that have been reproduced from Haupt et al. (2023) are noted in the respective captions.

80 We note that the study considers a single case study for a specific topic; thus, it is unclear whether the resulting findings generalize to other cases and atmospheric phenomena. However, we explore fundamental differences in mesoscale and microscale simulation techniques that are generally applicable for other atmospheric studies.

Section 2 discusses the observational dataset and various SST products that are included in this study. The model setup and computational discussion can be found in Section 3. Results are shown in Section 4, followed by a summary and discussion in Section 5 Sections 5 and 6, respectively.

## 85 2 Data and Methods

The modeled sensitivity of LLJ characteristics to SST is examined by including several auxiliary datasets. These datasets, which are produced from different satellite sensors, vary in spatial resolution and are described below.

### 2.1 Sea-Surface Temperature Datasets

90 The SST datasets used in this study are derived from varying underlying instrumentation, and are available at varying spatial and temporal resolution (Figure 1 and Table 1). Five SST datasets are downloaded from the Group for High Resolution Sea Surface Temperature Level-4 (GHRSSST-L4) database including: the Canadian Meteorological Center (CMC) analysis product (Canada

Meteorological Center, 2017), the Office of Satellite and Product Operations (OSPO) analysis (OSPO, 2015), the Multiscale Ultrahigh Resolution (MUR) dataset (NASA/JPL, 2015), the Naval Oceanographic Office (NAVO) dataset (NASA Jet Propulsion Laboratory, 2018), and the Operational Sea Surface Temperature and Sea Ice Analysis (OSTIA) analysis (UKMO, 2005).  
95 Additionally, an SST dataset from the Level-3 GOES-16 Advanced Baseline Imager (GOES-16) is downloaded from the GHRSSST database (NOAA/NESDIS/STAR, 2019) and gap-filled using Data Interpolating Empirical Orthogonal Functions (DINEOF) (Beckers and Rixen, 2003; Alvera-Azcárate et al., 2005; Beckers et al., 2006; Alvera-Azcárate et al., 2007).

Initial and boundary conditions for the model in this study are derived from the MERRA-2 reanalysis dataset (Global Modeling and Assimilation Office (GMAO), 2015e). Within the MERRA-2 dataset, SST comes from the OSTIA dataset  
100 (Figure 1a). Each auxiliary dataset overwrites skin temperature over water within the initial and boundary conditions for each simulation (Figure 1b–g). On the outermost domain for the GOES-16 simulations (Figure 1f), skin temperature is overwritten only over the area covered by domain-2 due to processing constraints. Because the spatial extent of domain-2 is large (600 km × 600 km) and encompasses the region of the ocean over which winds in this study are coming from, we expect this to have a negligible impact on the flow field over the region of interest. For every other setup, the satellite-derived SST products overwrite  
105 the skin temperature over water for the entirety of each domain.

Differences in the resolution of features between the various SST datasets is apparent (Figure 1). Most notably, the gradients in SST, which can be important forcing mechanisms for offshore LLJ formation (Gerber et al., 1989; Small et al., 2008; Whyte et al., 2008), are better captured at finer scales in the GOES-16 and OSTIA datasets (Figure 1f and e, respectively) than in the lower-granularity datasets such as NAVO and CMC (Figure 1b and c, respectively). OSPO (Figure 1d) and OSTIA (Figure 1e)  
110 share the same granularity, yet the features within the OSTIA dataset contain much finer detail. The MUR dataset has the finest granularity (Figure 1g) yet the resulting product appears much smoother than that of GOES-16 (twice the granularity) and even OSTIA (more than five-times the granularity). Note that while the native SST dataset within the MERRA-2 reanalysis product (Figure 1a) is produced from the OSTIA dataset (Figure 1e), the resolution of the MERRA-2 product is at the resolution of the MERRA-2 data at 0.62° latitude and 0.5° longitude. Based on the differences between these products, we expect to see  
115 differences in the simulated characteristics of the offshore LLJ such as in jet-nose height, maximum wind speed, and low-level shear.

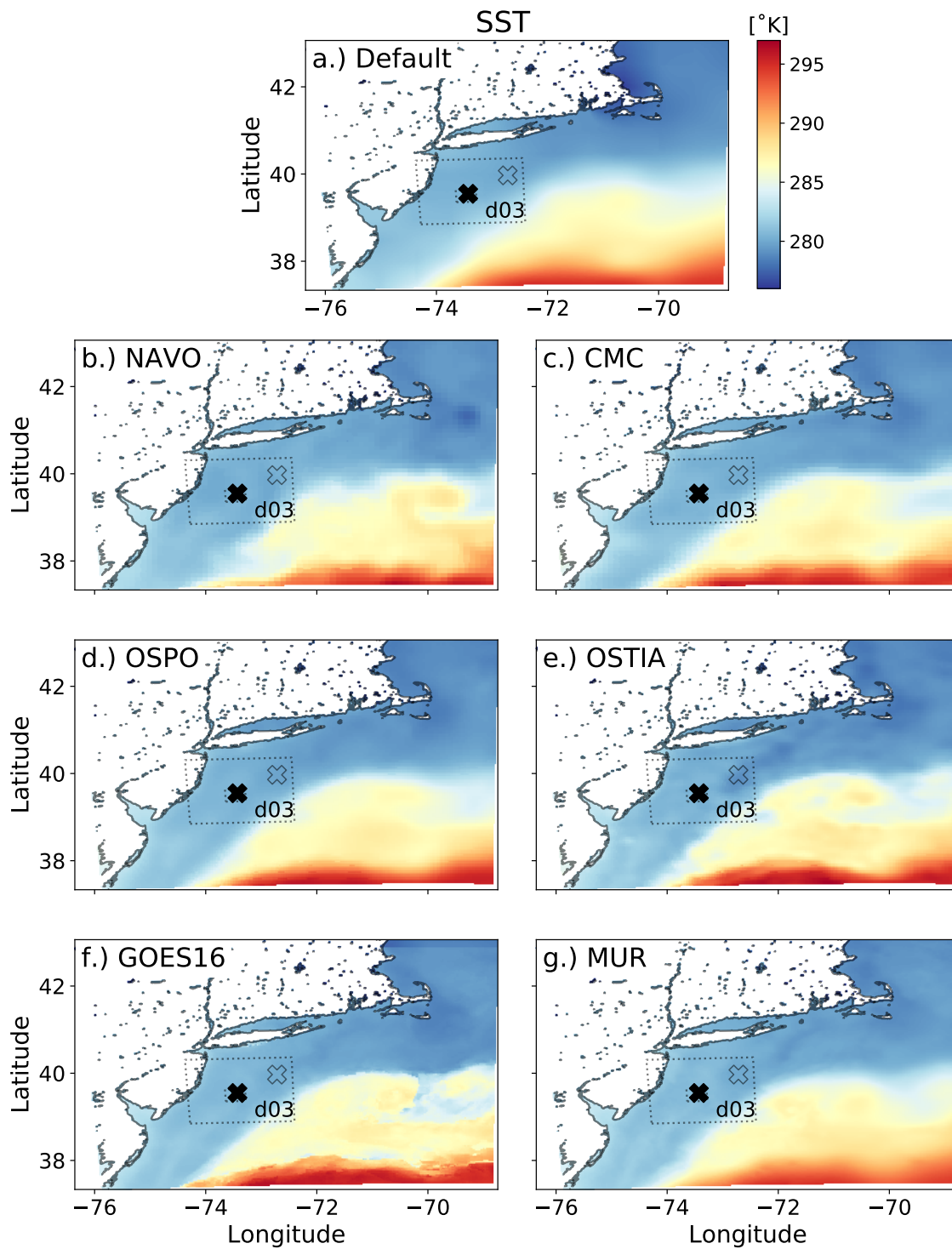


**Figure 1.** Sea surface temperature over domain 2 for each SST dataset. The locations of the E06 buoy (filled) and E05 buoy (open) are designated by an “X” in each panel. The outline of domain 3 is also shown with a dotted line. [This figure has been redrawn to include domain 3 from Figure 8 in Haupt et al. \(2023\).](#)

**Table 1.** Spatial granularity and types of sensors used in each WST dataset.

WST Dataset	Spatial Granularity (Lat. and Lon.)	Sensors
NAVO	0.1°	5 satellite sensors
CMC	0.1°	7 satellite sensors, drifting/moored buoys
OSPO	0.054°	6 satellite sensors, ships, drifting/moored buoys
OSTIA	0.054°	7 satellite sensors, drifting/moored buoys
GOES-16	0.02°	7 satellite sensors, drifting/moored buoys
MUR	0.01°	6 satellite sensors, drifting/moored buoys

## 2.2 Observations

In 2019, two EOLOS FLS200 floating lidar buoys were deployed in the New York bight by the New York State Energy Research and Development Authority (NYSERDA; OceanTech Services/DNV under contract to NYSERDA (OceanTech Services/DNV, 120 2019)). These buoys, named E05 and E06 (open and filled X in Figure 1, respectively), contain **vertical vertically** scanning lidars, ocean and wave sensors, and a small meteorological mast **recording atmospheric variables such as temperature and pressure**. Each lidar records data at 10 levels from 20 m to 200 m above mean sea level at 20 m increments. The data are **corrected for tidal variation and freely** available at 10-minute averaged output **. and are not corrected for wave or tidal variation. This correction has been shown to have a negligible effect in offshore floating lidar measurements when averaged at 10 minute** 125 **timescales (Krishnamurthy et al., 2023)**. While both E05 and E06 capture the event of focus, only data from E06 is considered within this study as explained in more detail in Section 3.

## 2.3 Analysis Metrics

To analyze model performance over the full rotor swept area, we consider an integrated parameter over the rotor layer: the rotor equivalent wind speed (REWS). The calculation of REWS with veer used in this study is defined in equation (9) 130 of Redfern et al. (2019):

$$\text{REWS} = \sum_{k=1}^N \frac{A_{ijk}}{A_T} |U_{ijk}| \cos(\theta_{ijk}) \quad (1)$$

where  $N$  is the number of layers within the total rotor swept area,  $A_T$ .  $A_{ijk}$  is the area of the rotor at a given level and  $U_{ijk}$  is the average wind speed at this level. Veer is taken into consideration through  $\theta_{ijk}$ ; the difference between the wind direction at hub height and the average wind direction in a given layer.

135 In this study we define the ensemble as the different SST setups for each domain (i.e., 7-member ensembles on each domain). We analyze the ensemble mean of individual variables and metrics (denoted by angle brackets), spread (Equation 2, where  $N$  is the number of ensemble members), and ensemble mean error (EME; Equation 3) every 10 minutes. Note that the purpose of this ensemble is not to estimate the error, so we do not expect the values of these metrics to be similar.

$$140 \text{ Spread} = \sqrt{\frac{1}{N} \sum_{j=1}^N (\text{member}_j - \text{Ens. Mean})^2} \quad (2)$$

$$\text{EME} = \sqrt{(\text{Obs.} - \text{Ens. Mean})^2} \quad (3)$$

## 2.4 Low-level jet case

The case study of interest in this work consists of an offshore LLJ that developed in the evening of April 5, 2020 off the coast of the Mid-Atlantic states, USA (data from the E06 buoy is shown in Figure 2). The jet begins as dominant wind direction in this case was from the South indicating the possibility of warm air advection as is commonly seen in the region (De Jong et al., 2024). While there exist many techniques to detect low-level jets from wind profiles (see, for example, Piety (2005) and Hallgren et al. (2023)), the observed low-level jet was detected using the technique described in Debnath et al. (2021). This algorithm detects a low-level jet based on meeting three criteria: (1) the maximum wind speed is not at the first or last lidar level, (2) the level of shear between the lowest lidar level and maximum wind speed is above  $0.035 \text{ s}^{-1}$ , and (3) the wind speed drop off between the maximum wind speed and top lidar measurement is greater than  $1.5 \text{ m s}^{-1}$  and the drop-off is more than 10% of the maximum wind speed. The jet begins as 2-m air temperature begins to rise and SST slowly decreases. The difference in 2-m air temperature and SST,  $\Delta T$ , serves as a proxy for atmospheric stability, where when positive one can expect stable atmospheric conditions. As the air and sea surface temperatures diverge and  $\Delta T$  grows larger, a strengthening in wind speeds occurs around 100 m and eventually leads to the formation of an LLJ. Over the six-hour period of interest beginning at 00Z on April 6 (8 PM local time on April 5), the jet nose remains at  $\sim 120 \text{ m}$  at the E06 buoy location with maximum wind speeds around  $16 \text{ m s}^{-1}$ . The LLJ persisted for several hours before weakening as  $\Delta T$  decreased towards zero with the passing of a cold front. This case was selected due to the clear and consistent LLJ signal and the apparent dependence on the air-sea temperature gradient.

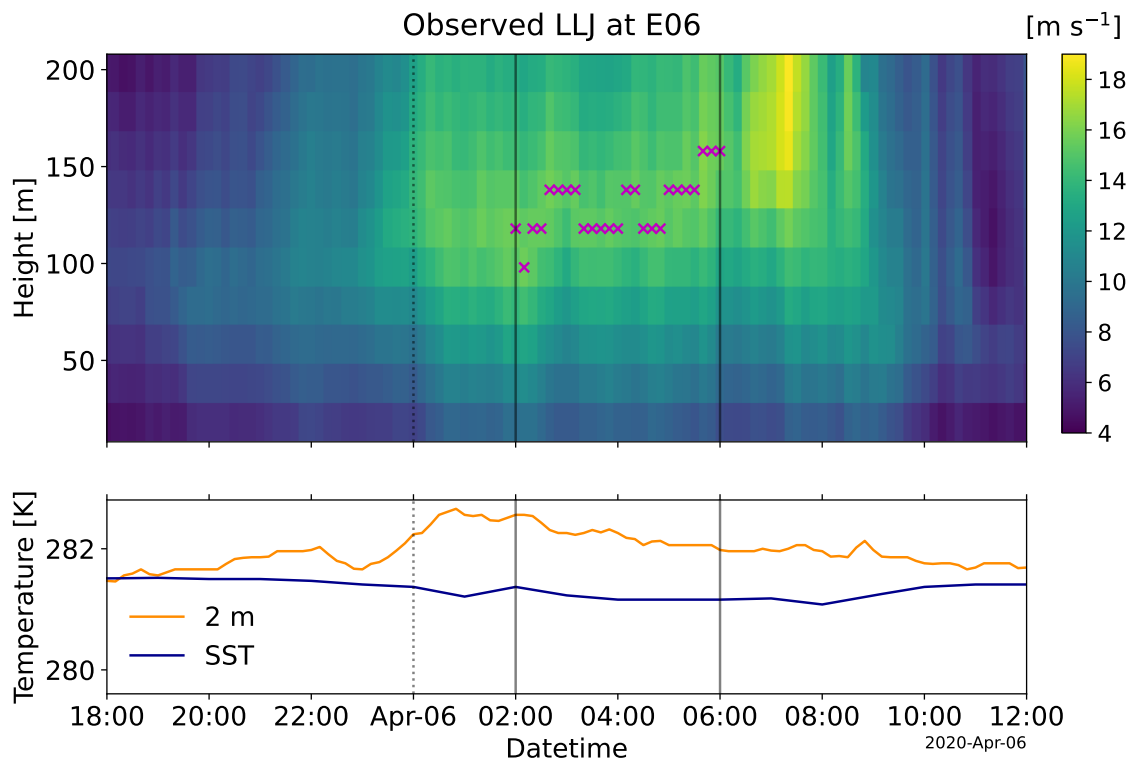


**Figure 2.** Observed wind speed from the E06 lidar (a) and 2 m 2-m air temperature and SST from the E06 buoy (b). Dotted vertical lines are the start of the LES simulations and solid vertical lines denote the period of interest. Magenta markers denote the jet height.

### 3 Model Setup

160 Simulations in this study were conducted using the Weather Research and Forecasting (WRF) model version 4.3 (Skamarock et al., 2021). Each simulation comprised five one-way nested domains with model horizontal grid spacing,  $\Delta_x$ , set to 6,250 m, 1,250 m, 250 m, 50 m, and 10 m on domains 1 through 5, respectively (Figure 3). Note that even with a  $\Delta_x$  of 10 m, we are likely not fully resolving the inertial subrange of the stable boundary layer and associated low-level jet (Beare and Macvean, 2004; Beare et al., 2006). Simulations at higher resolutions (down to sub-meter grid spacing) have not shown clear convergence in simulating the very stable boundary layer (Sullivan et al., 2016) and a small ensemble of cases at these resolutions is out of the scope of this current project. We do not anticipate the overall findings from this study to be impacted by the use of 10 m horizontal grid spacing as all simulations are equally impacted.

165

LES domains 4 and 5 are positioned with the E06 buoy in the northeast portion of the domain so that the incoming south-westerly flow has ample space to develop turbulence. Due to the spacing between the two floating lidars, it would be very difficult to run simulations with LES domains spanning both lidars. Thus, in this study, we focus strictly on data from the E06

170 lidar.

Model time step on domain 1 is set to 15 seconds and we use a time-step ratio of 3, 5, 5, and 5, for each nest. The vertical grid contains 131 levels with 21 levels below 200 m. The same vertical grid is defined for each domain such that vertical resolution is held relatively constant between each domain. Each domain also shares the following parameterizations: the revised Monin-Obukhov surface layer scheme (Jiménez et al., 2012), Ferrier microphysics (Ferrier, 2004), RRTMG longwave and shortwave radiation (Iacono et al., 2008), and the unified Noah surface layer model (Tewari et al., 2004). Domain-1 uses the Kain-Fritsch cumulus parameterization (Kain, 2004) and four-dimensional data assimilation (Liu et al., 2005, 2007; Reen and Stauffer, 2010). Turbulence closure on domains 1 and 2 is performed with the MYNN 2.5 planetary boundary layer scheme (Janjić, 2002). These domains will be referred to as the *mesoscale* domains. Domains 3–5 utilize the 1.5 order SGS turbulent kinetic energy (TKE) scheme (Deardorff, 1980) and are considered the *microscale* domains.

Simulations are initialized with the MERRA-2 reanalysis dataset as initial and boundary conditions (Global Modeling and Assimilation Office (GMAO), 2015a, b, c, d, e, f) at 06 UTC on April 4, 2020 and are run for 48 hours. [The European Centre for Medium-Range Weather Forecasts \(ECMWF\) v5 reanalysis \(Hersbach et al., 2020, ERA5\) dataset was also tested and performance with MERRA-2 was found to be slightly better for the specific case day considered here \(not shown\).](#) At initialization, only domains 1 and 2 begin. At 18 UTC on April 5, domain 3 initializes and the three domains are run for six hours. Finally, at 0 UTC on April 6, domains 4 and 5 initialize and the five-domain setup runs for an additional six hours (dotted black vertical line in Figure 2). We utilize the stochastic cell temperature perturbation method on all boundaries of domains 4 and 5 (Muñoz-Esparza et al., 2014, 2015) to accelerate turbulence development. The first hour of the simulations are considered spin up then the final five hours of simulation are considered for analysis (between the solid black vertical lines in Figure 2). Due to the computational expense of these runs, each simulation must restart after 20 minutes of simulation time while all five domains are running. Each domain produces output every 10 minutes to match the output frequency of the observations. Pseudo-tower (the *tslist* option in WRF) output was also produced at the location of the E06 tower for higher-temporal resolution analysis. However, in running the simulations for this study, an issue within the WRF pre-processing system (WPS) was found that impacted the LES domains; specifically the COSALPHA and SINALPHA calculation (Figure A2) and corrupted the ~~psuedo-tower~~ [pseudo-tower](#) (*tslist*) output. This issue is explained in more detail in Appendix A along with an analysis of the impact on the model solution (Figure A1). Within this manuscript, we refer to a *setup* as all domains in a simulation for a single SST product.

[The simulations were run on the NSF National Center for Atmospheric Research \(NCAR\) Cheyenne supercomputer. To provide evidence of the computational expense of LES for real-data cases, the following information is provided. Each LES run required 1,296 cores running for between 11 and 12 hours of wall-clock time in order to produce 10 minutes of simulation. Thus, to run for the full 6 hours, 35 restarts were required to fit within the Cheyenne 12-hour job limit. In total, this results in between 513,000 to 560,000 core hours per LES simulation – 3.6-3.9 million core hours in total.](#)

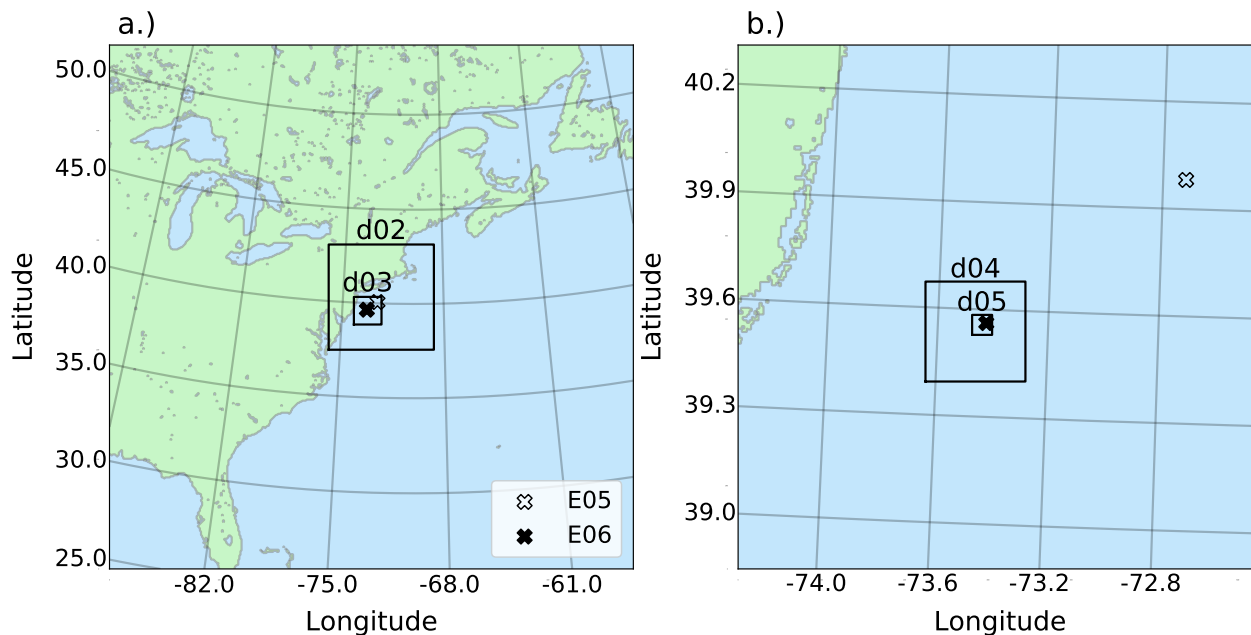


**Figure 3.** Domain configuration within WRF. The locations of the E06 buoy (filled) and E05 buoy (open) are designated by an “X” in each panel. The outer extent of (b) is the perimeter of domain 3.

#### 4 Results

The following results are derived from each simulation at the location of the E06 buoy for all domains. For domains 1 and 2 – the mesoscale domains – data is extracted from the single cell that encompasses the E06 buoy location. For domains 3, 4, and 5 data is spatially averaged over a block of cells that are centered over the E06 buoy location and cover the footprint of one domain-2 cell. This is done to average the turbulent results on the microscale in order to compare the mesoscale and LES results more faithfully. While domains 4 and 5 are considered LES or microscale domains, domain 3 has a grid spacing of 250 m, which is within the *terra incognita* (Wyngaard, 2004) or gray zone. LES turbulence *closure* techniques are used in this study within this domain *though the appropriateness of this modeling technique is questionable although its appropriateness is questionable due to the fact that the largest energy-containing eddies are not fully resolved with this grid spacing*. The other option is to use a planetary boundary layer scheme at this resolution, but the *assumptions of horizontal homogeneity and that all energy-containing eddies are unresolved renders the* applicability of such parameterizations at 250 m grid spacing are *even yet* more questionable. An investigation of the applicability of a three-dimensional PBL scheme in WRF (Kosović et al., 2020; Juliano et al., 2022; Eghdami et al., 2022) within this domain may shine light on using such a scheme as a potential alternative moving forward.

Analysis focuses on the representation of the wind field and characteristics of the simulated jet when augmenting the SST dataset (as discussed in Section 2) that is ingested into WRF. The observations in this study are limited to 10-minute averaged

wind profiles over time, measurements of temperature at 2 m, and SST. Thus, the simulation datasets are also averaged at 10-minute intervals for comparison with observations. The offshore wind turbine specifications assumed in this study consist of a hub-height of 118 m with a rotor diameter of 160 m. These dimensions are similar to typical offshore wind turbines currently installed as of the writing of this paper (Stehly and Duffy, 2021; Musial et al., 2023). Analysis of SST and low-level jet characteristics is performed first. Ensemble statistics are then calculated in order to determine the sensitivity of the jet characteristics to SST and how that sensitivity changes across domains. Lastly, it is determined whether selecting the single best-performing mesoscale setup for driving LES will provide the best solution on the microscale for this low-level jet case. It is important to note that one could run a suite of model configurations for the microscale domain for each SST setup in order to improve the microscale model simulation associated with each mesoscale simulation. In practice, however, the LES simulations are very computationally expensive to run as previously mentioned. Thus, in this study, we select a single LES configuration and run it for each SST setup – for better or for worse – to emulate a real-world scenario in which only a mesoscale suite of simulations is run that is used to determine the best single SST setup to drive an LES simulation.

#### 4.1 SST Depiction

For each simulation, the average modeled SST value at the E06 buoy may vary from domain to domain (Figure 4). This is more apparent when the higher-resolution SST datasets (GOES-16 and MUR) are employed. For the lower-resolution domains and default SST dataset, SST may differ between domain 1 and domain 2, but values for domains 3-5 are very similar. Note that each dataset depicts colder SST values than what was observed.

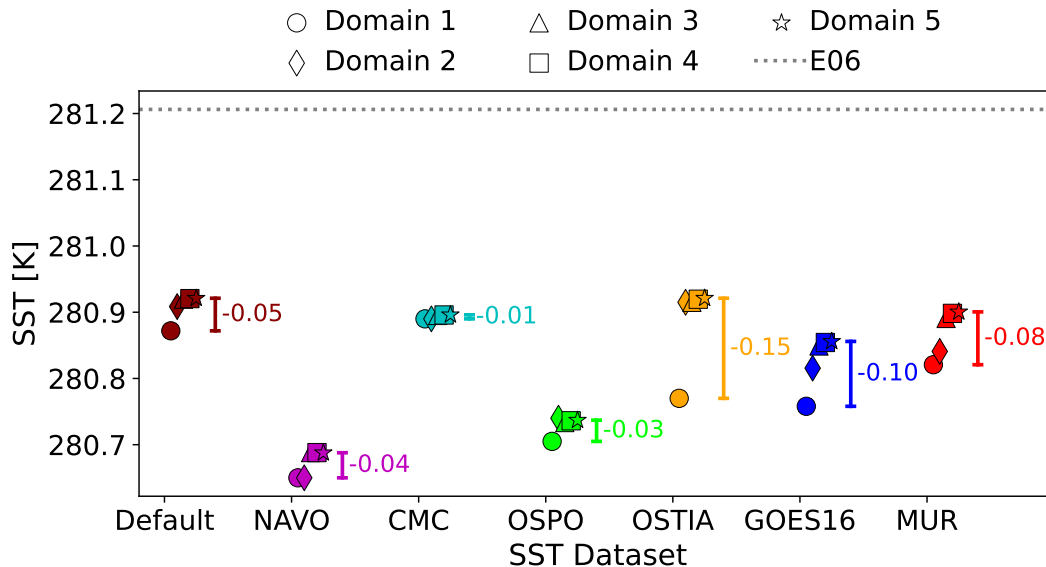


**Figure 4.** Average SST for each setup and each domain along with the difference between SST on domain 1 and domain 5.

## 4.2 Low-level Jet Characteristics

Low-level jets have historically been detected via a vertical profile of wind speed in which a maximum is reached at some height above the surface followed by a decrease in wind speed above that level. For **wind** the purposes of this study, we do not enforce requirements on the simulated low-level jets to meet certain thresholds for the amount of shear and drop-off in wind speeds above the jet nose in order to consider them “low-level jets”. Simply, for the simulations, the height of maximum wind speed is used to define the low-level jet height.

For **wind** energy purposes, shear – the difference in wind speed over a certain height,  $dU/dz$  – is often considered over the rotor swept area. In this study, we will consider a rotor swept area from 38 m to 198 m (solid black lines in Figure 5). We define low-level shear as **the bulk** shear between the bottom of the rotor swept area (38 m) and hub-height (118 m; dashed line in Figure 5).

During the period of interest, a **wind speed maxima** maximum wind speeds are observed between 80 and 150 m is observed (Figure 5a). On the mesoscale domains (Figure 5b and c), a maximum wind speed is reached around 200 m. (There is a decrease in wind speed above this height in the mesoscale domains confirming that this is a low-level jet profile; not shown.) At low levels, the mesoscale simulations (Figure 5b and c) often produce higher wind speeds than in observations (Figure 5a). Here, low-level shear within the mesoscale simulations is too weak. The gray zone and microscale domains (Figure 5d–f) recover the jet profile and bring the jet maxima down to levels near, but slightly higher than in observations. The low-level wind speeds are much closer to observations, but with a stronger jet maximum wind speed resulting in stronger shear than than observed. In each of the simulations, the LLJ peaks around 160 minutes before seen in the observations (see Figure 2 for comparison). When shifting the observations **in time** to better match with simulated results (not shown), some metrics are slightly improved but the overall message remains unchanged. The same can be said for changing the period of interest to several 3–5 hour intervals between 01 UTC and 06 UTC (not shown).

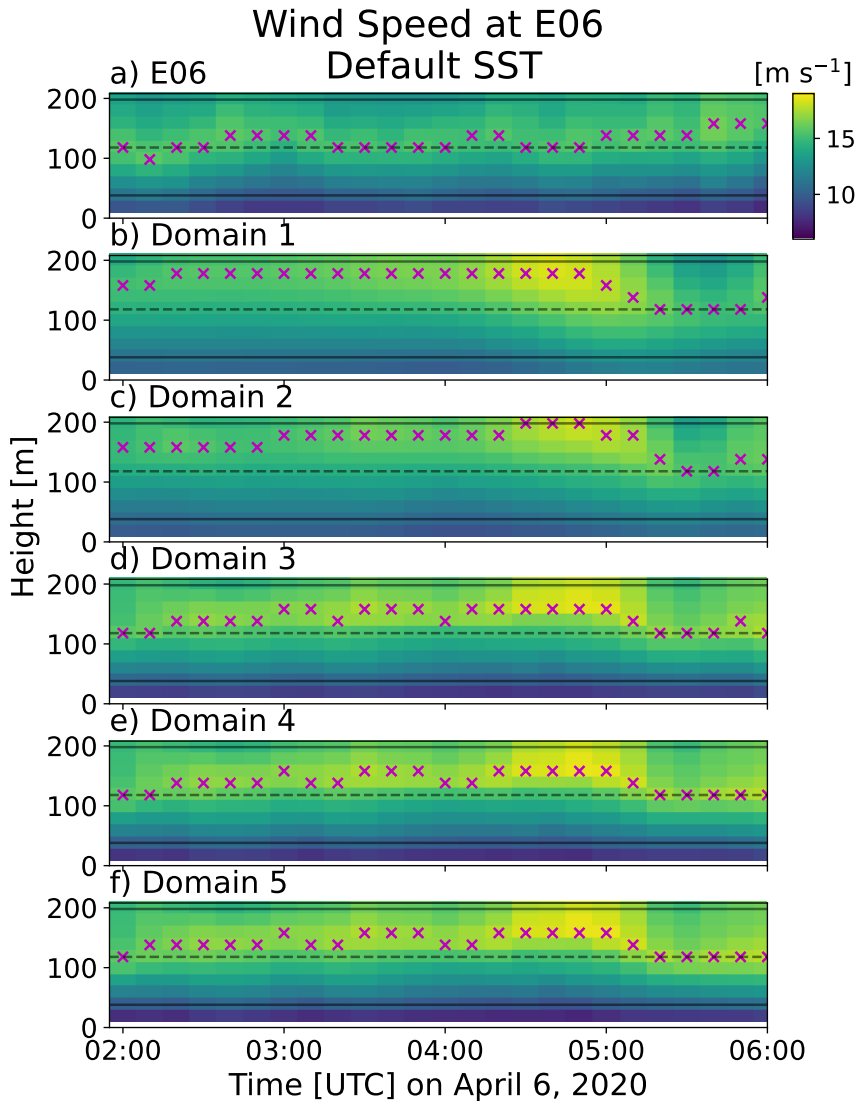


**Figure 5.** Vertical profiles of wind speed with time for observations (a), and domains 1, 2, 3, 4, and 5 (b–f, respectively) for the Default SST setup during the period of interest. Magenta markers denote the jet height. The assumed hub height (dashed line) and rotor layer (between the solid lines) in this study are also shown.

Comparing hub-height wind speeds for each SST setup (Figure 6) displays some subtle variability as SST is augmented between the datasets, but significant variation exists between domains within a setup. The differences between the mesoscale domains (shades of red) is larger than between the two LES domains (shades of blue), which follow each other closely. Domain 3 hub-height wind speeds fall in between that of domains 2 and 4 but more closely resemble the LES solutions. This pattern is also shown when analyzing the root mean squared error (RMSE) and bias of hub-height wind speed (Figure 7a and d). RMSE and bias between the mesoscale domains are similar, while the resulting RMSE and bias on

265 domain 3 is quite different from that of the mesoscale domains. Then, on the microscale domains, there is not much of a  
change between the RMSE and bias for hub-height wind speed.

270 The gray zone and LES domains generally improve the simulation of hub-height wind speeds for much of the period of  
interest (Figure 6). Towards 05 UTC these wind speeds increase to well above what was observed. The mesoscale domains  
are deficient in hub-height winds for the majority of the period but increase to around what was observed at 05 UTC. During  
this ramp up in wind speeds, domain 1 wind speeds often increase well beyond those observed while domain 2 wind speeds  
remain much closer to the lidar wind speeds. Overall, the bias on the mesoscale domains remains positive while  
on domain 3 and the microscale domains the bias is negative (Figure 7d). For many setups, we see improvement in hub-  
height wind speed predictions as grid spacing increases with jumps in the gray zone with a jump in performance occurring  
between the mesoscale domains and when transitioning from mesoscale to LES on domain 3.

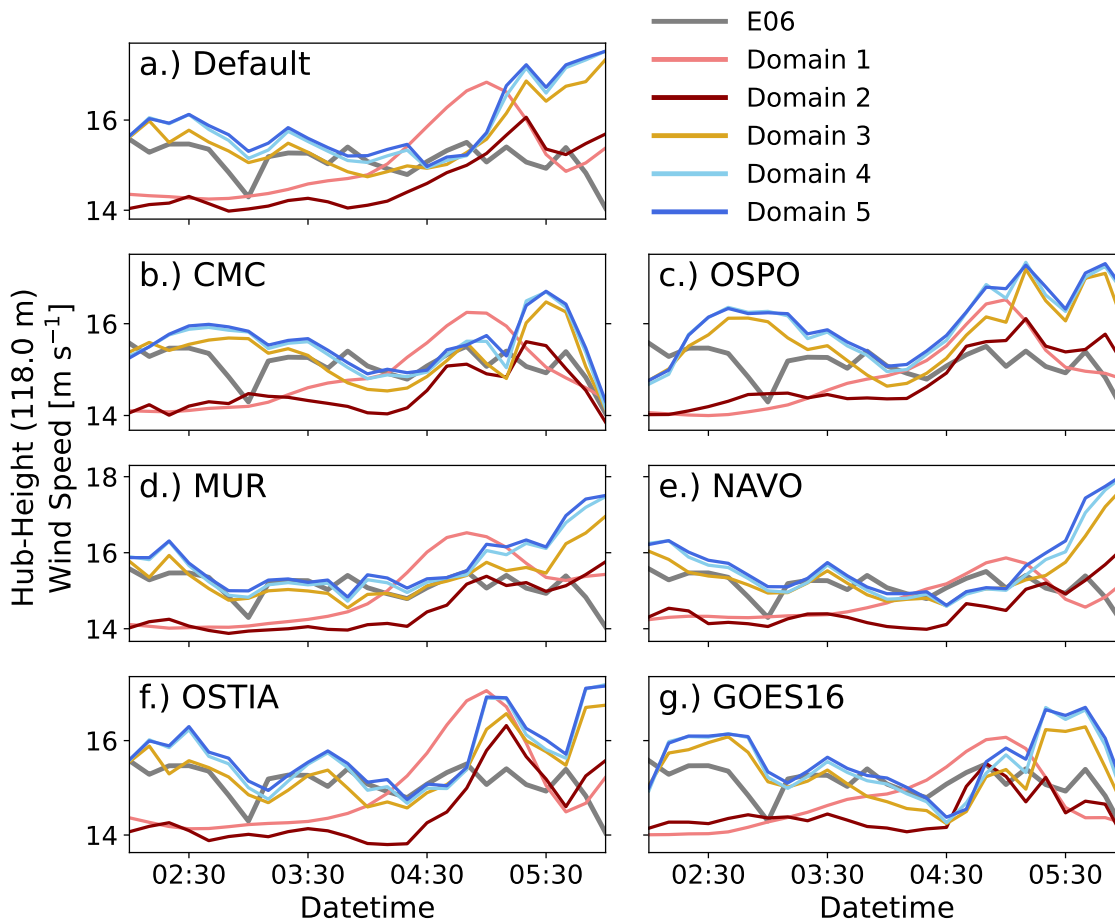


**Figure 6.** Hub-height wind speed for the mesoscale (shades of red), gray zone (yellow), and microscale (shades of blue) domains for each SST setup along with the observed hub-height wind speed (grey).

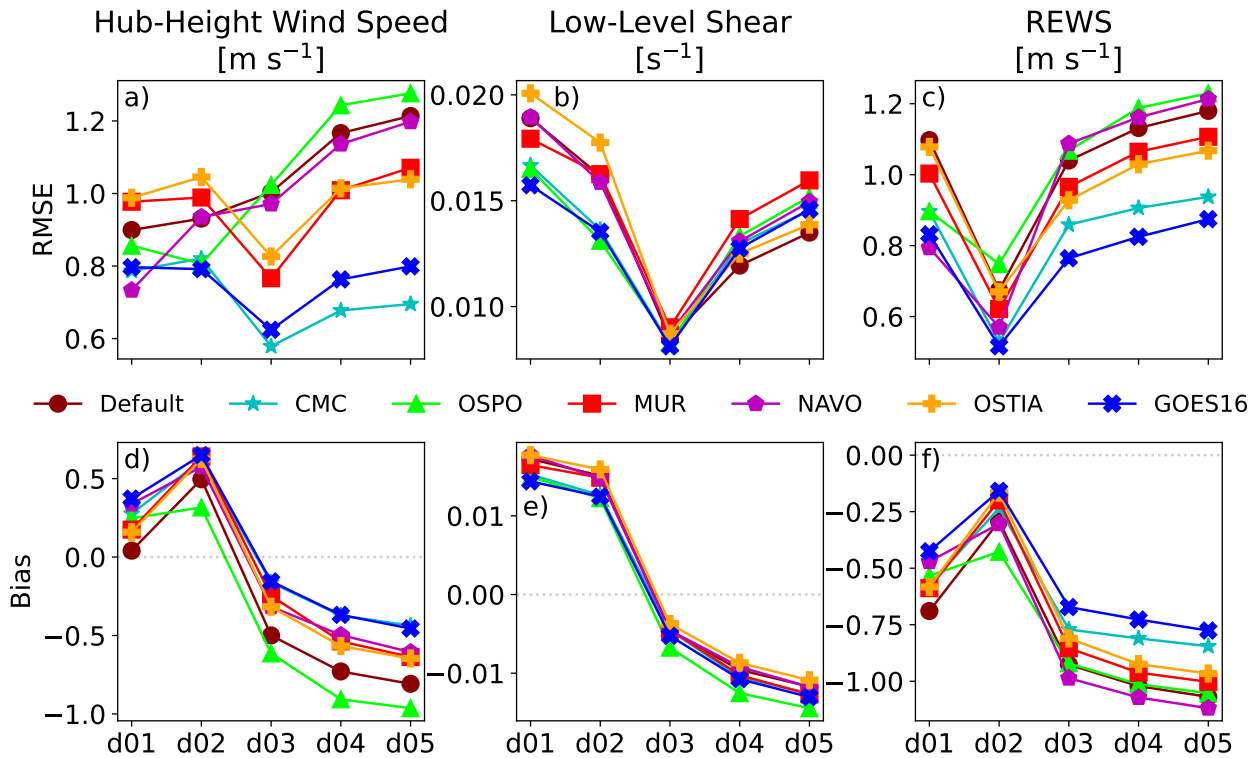


**Figure 7.** Root mean square error and bias for the mesoscale and microscale domains for all setups of low-level shear, hub-height wind speed, and rotor equivalent wind speed (REWS). This figure has been redrawn to include REWS from Figure 9 in Haupt et al. (2023).

275 Prediction of low-level shear generally improves when moving from the mesoscale domains to LES with, again, a large jump  
in performance on domain 3 (Figure 8 and Figure 7b and e). The mesoscale domains under-predict the low-level shear while  
LES domain predictions come closer to the observed shear, but are too large. The gray-zone results are closest to observations  
in all SST setups. For the performance on the LES domains, this is mostly due to wind speeds being too low at the bottom of  
the rotor layer (Figure 8). For the mesoscale domains, wind speeds at the bottom of the rotor layer are faster than observed  
280 while wind speeds at hub-height are too slow. Domain 3 benefits from slightly faster wind speeds than LES at lower levels, but  
similar wind speeds at hub-height, which produces more accurate predictions of low-level shear. Again, the variability across  
the mesoscale domains is larger than between the microscale domains.

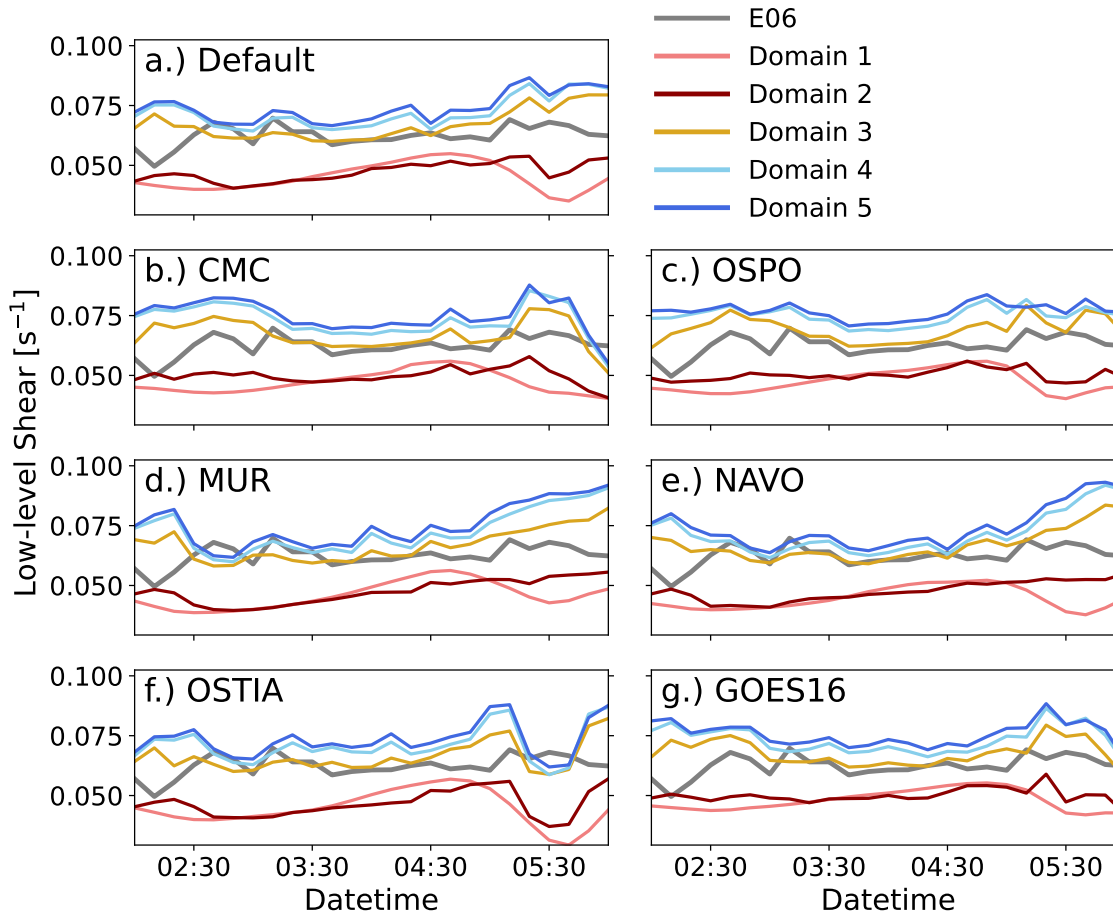


**Figure 8.** Same as Figure 6 but for low-level wind shear.

Model performance considering REWS (Equation 1) improves in each setup from domain 1 to domain 2 (Figure 7c and f). The largest change in performance, as with the other variables, occurs on domain 3 in which RMSE increases and bias becomes more negative with the worst performance occurring on domain 5 in each setup. This is due to the over-prediction of wind speeds at and above hub-height within the microscale domains and domain 3.

Note that the wind speeds modeled are in the rated portion of most wind turbines. For reference, if we were in the cubic portion of the power curve, over-prediction of wind speeds by this amount would result in over-predictions of energy production during this period by between 3–16% for the mesoscale domains and between 15–27% on domain 3 and the LES domains (assuming wind speeds are below rated wind speed and above the cut-in speed, a performance coefficient of 0.4, and an average air density of 1.225 kg m<sup>3</sup>).

### 4.3 Surface Forcing Characteristics

295 Simulated low-level jets are highly dependent on surface forcing characteristics. If the surface forcing is inaccurate, then the resulting low-level jet can be expected to be inaccurate. Comparing simulated 2 m temperature against observations, we see that for every setup the RMSE decreases from the mesoscale domains to domain 3 while bias is also reduced to be closer to zero (Figure 9a and d). Once on the microscale domains, RMSE increases and bias becomes more positive; close to what was seen on domain 1. RMSE and bias of SST improve in most setups between domain 1 and domain 3, but then remain relatively constant on the microscale domains (Figure 9b and e).

300 Analyzing 2 m temperature and SST alone do not depict the true surface forcing conditions. For that, we analyze  $\Delta T$ , as discussed in Section 2.4. Although the biases in both 2 m temperature and SST are positive, the differences between the two are larger than what is observed (Figure 9f) producing a negative overall bias for each setup on nearly all domains. RMSE is largest on domain 3 for each setup and then reduces on the microscale domains (Figure 9c).

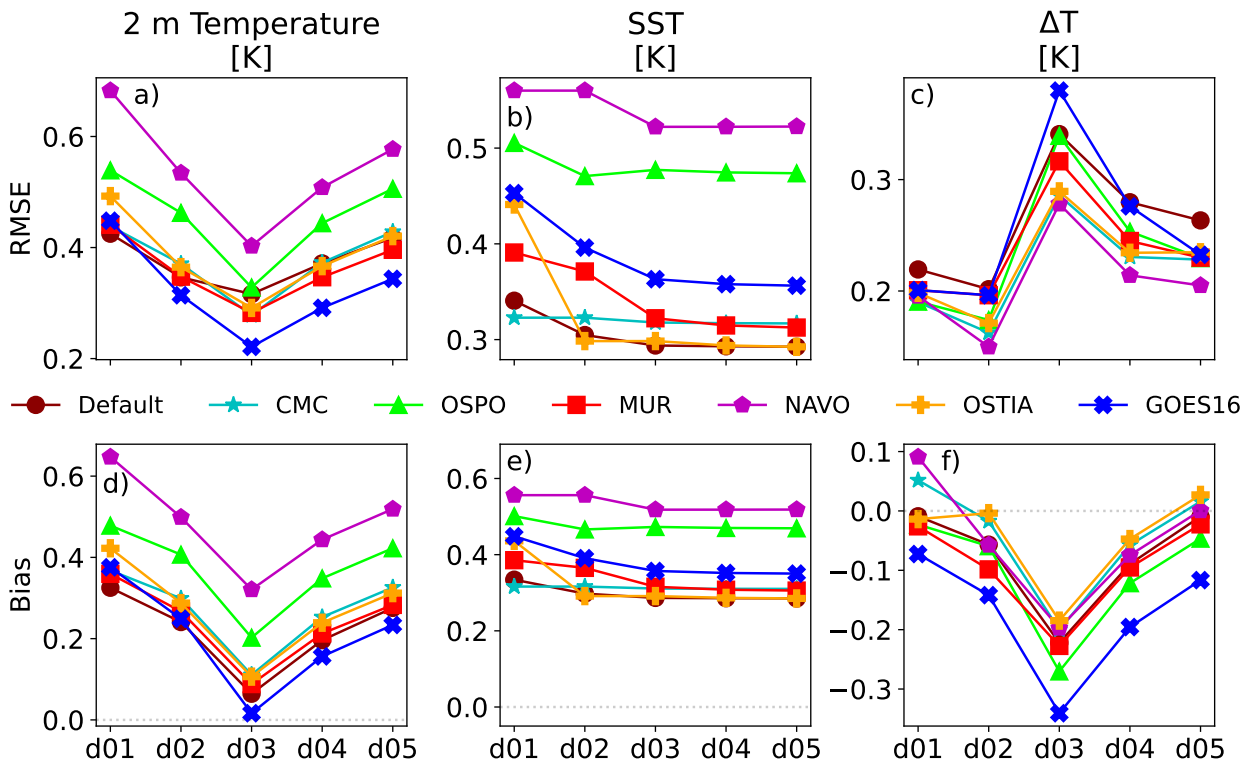


**Figure 9.** Same as Figure 7 but for 2-m temperature, SST, and  $\Delta T$ . While SST is defined from the input SST datasets, both 2 m temperature and the resulting  $\Delta T$  are predicted within the model.

#### 4.4 Ensemble Statistics

305 In order to quantify model sensitivity to SST across scales, it is helpful to consider results from all SST setups together as opposed to on a setup-by-setup basis. Recall that “setups” refers to the set of simulations run with varied SST datasets.

Ensemble results are generated on each domain by averaging data from all setups. Here we analyze the ensemble mean of individual variables and metrics (denoted by angle brackets), spread (Equation 2, where  $N$  is the number of ensemble members), and ensemble mean error (EME; Equation 3) every 10 minutes. Note that the purpose of this ensemble is not to estimate the error, so we do not expect the values of these metrics to be similar.

$$Spread = \sqrt{\frac{1}{N} \sum_{j=1}^N (member_j - Ens.Mean)^2}$$

310  $EME = \sqrt{(Obs. - Ens.Mean)^2}$

The vertical profile of the ensemble mean wind speed is drastically different between the mesoscale domains and LES domains over time (Figure 10a–c). On average, the LES domains slightly under-predict wind speed at low levels and over-predict the jet height and jet maximum wind speed (Figure 10d). Meanwhile, the mesoscale domains produce lower amounts of vertical shear and over-predictions of jet nose height. Further, the range in values over all SST setups on the LES domains is often much larger than that on the mesoscale domains (Figure 10a–c). This produces a larger time-averaged spread (denoted by an over-bar) throughout the lowest 200 m in the LES domains when SST is varied (Figure 10e). Notably, domain 3 has a similar spread to domains 4 and 5 at upper levels, but produces spread between the mesoscale simulations and remaining LES simulations below the jet nose. Increasing the model resolution from domain 1 to domain 2 results in an increase in spread of wind speed throughout the majority of the profile.

320 EME, averaged in time, is reduced near the surface as resolution increases from domain 1 through to domain 3, but then begins to increase again from domain 4 to domain 5 (Figure 10f). Above the observed jet nose, EME on the LES domains increases rapidly. This increase in error is mostly attributed to an over-prediction of maximum wind speed with an over-prediction of jet height. The mesoscale domains do not represent the shear and jet height well, but produce lower error by not over-shooting wind speed and over-predicting the jet height.

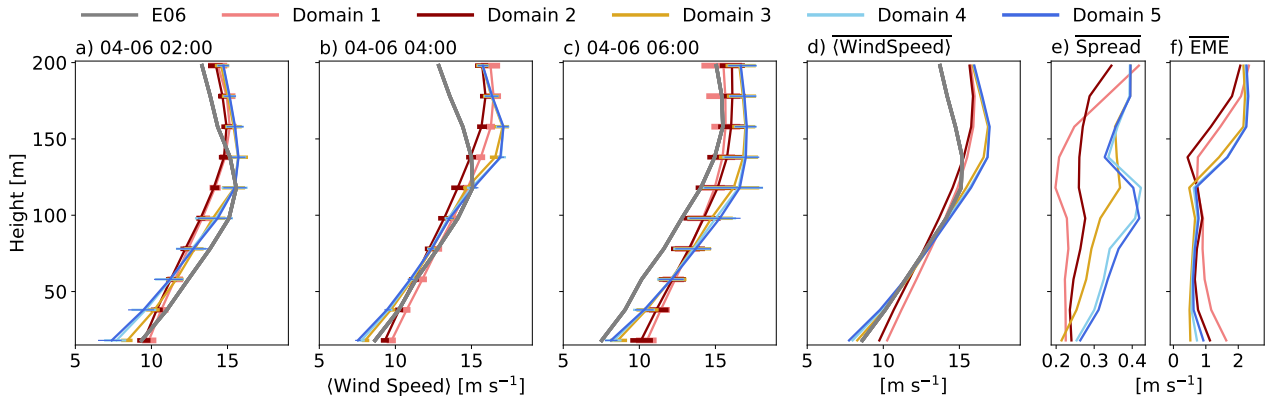


**Figure 10.** Vertical profiles of ensemble averaged wind speed at different times (a–c) for the mesoscale (shades of red), gray zone (yellow), and microscale (shades of blue) domains along with observations (grey). Error bars denote the spread between SST setups. The time-averaged ensemble average wind speed (d), spread (e), and ensemble mean error (EME; f) are also shown.

325 Changes in SST also generate larger spread on the gray zone and LES domains for low-level shear and hub-height wind speed (Figure 11a and c, respectively). Additionally, EME for these variables is also reduced as compared to the mesoscale domains for much of the period of interest on the gray zone and LES domains (Figure 11b and d, respectively).

Above hub height, spread increases for the mesoscale domains and error on the LES domains is higher than the mesoscale (Figure 10e and f). For this reason, we consider an integrated parameter over the rotor layer, the rotor equivalent wind speed (REWS), in order to determine the total impact of these variations within the environments considered important for wind energy. The calculation of REWS with veer used in this study is defined in equation (9) of Redfern et al. (2019):

$$REWS_d = \sum_{k=1}^N \frac{A_{ijk}}{A_T} |U_{ijk}| \cos(\theta_{ijk})$$

where  $N$  is the number of layers within the total rotor swept area,  $A_T$ .  $A_{ijk}$  is the area of the rotor at a given level and  $U_{ijk}$  is the average wind speed at this level. Veer is taken into consideration through  $\theta_{ijk}$ ; the difference between the wind direction at hub height and the average wind direction in a given layer.

When considering the wind speed over the rotor swept area, spread on all domains is very similar (Figure 11e). EME of REWS is lowest on domain 2 and highest on the LES domains (Figure 11f). The mesoscale domains benefit from slightly under-predicting wind speeds below hub height and over-predicting wind speeds above 100 m, the mesoscale domains do not over-predict the wind speeds as much as the LES domains do above the jet height (Figure 10d), which reduces error in REWS.

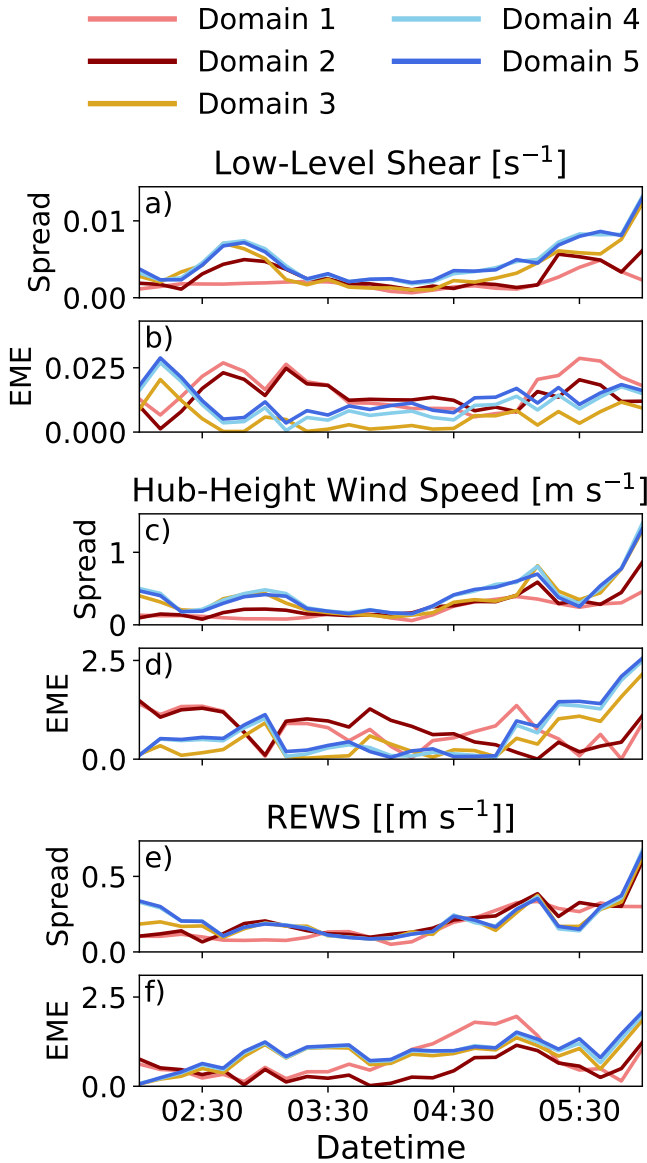


**Figure 11.** Spread and ensemble mean error on the mesoscale (shades of red), gray zone (yellow), and microscale (shades of blue) domains for low-level shear (a and b), hub-height wind speed (c and d), and rotor-equivalent wind speed (e and f).

340 Analyzing the time series of the ensemble mean of bias in low-level shear (Figure 12a) the mesoscale domains under-predict low-level shear while LES domains over-predict. The gray zone domain minimizes bias due to producing slightly faster near-surface wind speeds than the LES domains. In order to determine if increased stability is the cause of this disparity, the temperature difference between  $2_m$   $2-m$  temperature and SST,  $\Delta T$ , is calculated (Figure 12b). While  $\Delta T$  is not a perfect metric for stability, it is possible to compare the model against observations using this metric to glean some insight into the near-

surface stability. The bias for  $\Delta T$  on each domain is similar until late in the period of interest.  $\Delta T$  bias is predominantly near  
345 zero or ~~positive~~ **negative** indicating stronger stable conditions in the simulations. This is confirmed by examining surface sensible  
heat flux (SHFX; Figure 12c) where the values are negative throughout the period. It is interesting to note that the mesoscale  
domains produce larger negative values of SHFX than the LES domains, which indicates more stable conditions. **This is  
reinforced when checking the potential temperature profiles in which the lapse rate near the surface for the mesoscale  
domains is stronger than that of the LES domains (not shown).** In more stable conditions, one might expect shear to be  
350 stronger at low levels (Holtslag et al., 2014); this is not the case in these simulations. For the majority of the period of interest,  
domain 1 produces a larger negative value of SHFX than domain 5 until around 0530 UTC when the SHFX values become  
similar. Inspecting low-level shear bias, the differences between domain 1 and domain 5 remain fairly constant throughout  
the period of interest. When the sudden increase in SHFX on domain 1 occurs (bringing the value close to that of domain 5),  
the difference in low-level shear bias is actually increased even though SHFX values become similar. This suggests that the  
355 separation in performance of low-level shear bias appears to be more closely related to whether the domain is a mesoscale  
or microscale domain rather than the actual value of SHFX. It is possible that the PBL scheme on the mesoscale domains is  
over-mixing. It is also possible that the drag forcing over water on the LES domain is misrepresented, resulting **in** shear being  
too strong at low levels. This is discussed in more detail in Section **56**.

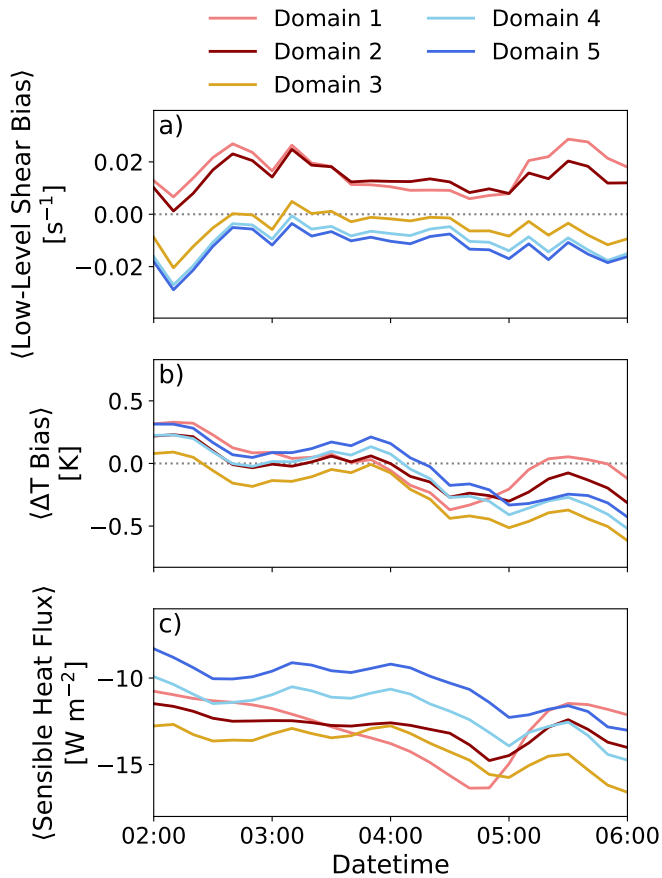


**Figure 12.** Ensemble means of low-level shear bias (a),  $\Delta T$  bias (b), and surface sensible heat flux (c), for the mesoscale (shades of red), gray zone (yellow), and microscale (shades of blue) domains.

#### 4.5 Predicting Performance Across Scales

360 Running an ensemble of LES is computationally expensive. To save computational resources and maximize model performance, it is logical to perform various simulations varying components of the model (e.g., parameterizations, initial and boundary conditions, etc.) on the mesoscale in order to find the best model setup. This best setup can then be used to drive the LES run, which would be assumed to produce the best possible LES result from the available mesoscale setups. We recognize that the definition of “best” performer is subjective and likely to change based on the phenomena of interest as well as the metrics in which one is interested. Unless there is a single metric to be optimized, the comparison of simulation results requires consideration of several variables and weighting the performance based on the interests of the study at hand. That said, when assuming that the best mesoscale result will produce the best microscale result, we are assuming that each LES simulation will perform similarly as the parent mesoscale simulation that drives it. This in turn assumes that the spread between the mesoscale runs and LES runs will be similar; the same goes for ensemble mean error. It has been shown that ensemble error and spread

365

370 change among domains from the mesoscale to microscale, thus, we investigate whether we can safely assume that the best performing setup on the mesoscale will lead to the best performing microscale simulation.

Considering root mean square error (RMSE) and bias RMSE and bias with respect to observations for each setup on the mesoscale and microscale domains over the period of interest for a variety of variables, model performance can be assessed to determine the top mesoscale performers. The variables considered important in the context of wind energy here are: (1) low-level shear, 375 (2) hub-height wind speed, (3) REWS. On the mesoscale domains (domain 1 and domain 2), the lowest RMSE and smallest bias in low-level shear are from the OSPO, GOES-16, and CMC SST datasets (Figure 7a and d). The same three datasets produce the lowest RMSE for hub-height wind speed for domain 2, with only the NAVO dataset performing better on domain 1 (Figure 7b). Hub-height wind speed is under-predicted on the mesoscale resulting in negative biases for all SST setups (Figure 7e). Considering REWS, the CMC and GOES-16 datasets are among the top performers on the mesoscale domains, particularly domain 2, while OSPO is among the worst performers for REWS in error and bias (Figure 7c and f). On the other hand, the OSTIA dataset is 380 one of the worst performers on the mesoscale domains for each of these metrics with the exception of REWS bias. Thus, the following top performers for the mesoscale with respect to wind profile characteristics are identified as: GOES-16, CMC, and OSPO; and the worst performing ensemble member is OSTIA (see Table 2).

Root mean square error and bias for the mesoscale and microscale domains for all setups of low-level shear, hub-height wind speed, and REWS.

To select a single best performing mesoscale setup, one might also consider how well the low-level forcing variables are 385 captured in each setup. The low-level forcing variables considered here are: (1) 2 m 2-m Temperature, (2) SST, and (3)  $\Delta T$ . RMSE and bias of 2 m 2-m temperature at the E06 buoy location are best for the GOES-16 setup on the mesoscale domains while CMC and OSPO are in the mid-to-lower tier of performers (Figure 9a and d). For SST, CMC performs reasonably well while GOES-16 and OSPO are among the worst performers on the mesoscale domains (Figure 9b and e). The main driver for the surface forcing, however, is the difference between 2 m 2-m temperature and SST,  $\Delta T$ . The GOES-16 setup results in some 390 of the highest error and highest largest bias (Figure 9c and f) leading to the assumption that perhaps the mesoscale domains in this case were getting the right answer for the wrong reasons. Meanwhile OSTIA, the worst performing ensemble member for the mesoscale domain, captures  $\Delta T$  reasonably well with relatively low RMSE and the smallest bias. Of the three selected best mesoscale performers, CMC produces the best results for  $\Delta T$  on the mesoscale and could reasonably be chosen as the setup to drive the LES runs.

395 Ranking the performance is highly dependent on the specific feature being studied. For this context, we study, we consider performance of the dynamic variables above (low-level shear, hub-height wind speed, and REWS) and forcing conditions (2-m Temperature, SST, and  $\Delta T$ ) to rank the mesoscale performers, setup performance. Considering these variables and weighting them equally, we rank the mesoscale SST dataset performance from best to worst as follows: CMC, OSPO, GOES-16, Default SST, NAVO, MUR, OSTIA (Table 2).

400 Same as Figure 7 but for 2 m temperature, SST, and  $\Delta T$ . On the mesoscale domains (domain 1 and domain 2), the lowest RMSE and smallest bias in low-level shear are from the OSPO, GOES-16, and CMC SST datasets (Figure 7b and e). The same three datasets produce the lowest RMSE for hub-height wind speed for domain 2, with only the NAVO dataset performing better on domain 1 (Figure 7a). Hub-height wind speed is under-predicted on the mesoscale resulting in positive biases for all SST setups (Figure 7d).

405 When the simulation grid spacing enters the gray zone with an LES turbulence closure scheme, the results for the wind field (Figure 7) and near-surface forcing (Figure 9) change drastically (with the exception of SST in which little variation is found across all domains). Biases for low-level wind shear and hub-height wind speed jump from ~~negative to positive~~ ~~positive to negative~~ due to decreases in wind speed near the surface and higher wind speeds at the jet nose. RMSE of low-level shear reaches local minimum in all SST setups due to the near-surface wind speed being slightly faster than the LES domains while maintaining a similar wind speed at hub-height (Figure 10d). Similarly, ~~2 m temperature~~ ~~2-m temperature~~ RMSE reaches a local minimum on domain 3 while bias is nearest to zero for all SST setups (Figure 9a and d).

Considering now the LES domains, the temperature forcing field's performance recover from the step change in domain 3 to remain more or less static between the mesoscale and microscale (Figure 9). There are some adjustments in the ranked performance in these fields, but no large shifts from worst on mesoscale to best on microscale. From this, we might expect that performance in the important variables identified above would also not change dramatically.

For the wind profile characteristic variables, the best performers in low-level shear on the LES domains are the default SST setup and the OSTIA setup (Figure 7~~ab~~ and ~~ae~~). Recall that the OSTIA setup was the worst performer on the mesoscale. OSTIA also improves to be among the middle-to-top performers for hub-height wind speed and REWS (Figure 7~~ba~~, c, ~~cd~~ and f). GOES-16 and CMC performed at opposite ends of the spectrum for  $\Delta T$  yet produce similarly good results on both the mesoscale and microscale. Ranking the setups for microscale performance results in: CMC, GOES-16, OSTIA, MUR, Default SST, NAVO, OSPO (Table 2). Note that two of the top three performers on the mesoscale are the top two of the microscale performance ranking. However, OSPO moves from the second best overall performer on the mesoscale to the worst performer on the microscale. Likewise, the worst mesoscale performer improves to the third best performer on the microscale domain.

OSPO was one of the better performers for low-level shear and hub-height wind speed on the mesoscale. Depending on the metric that is most of interest to a study, it could have been selected as the best performing mesoscale study. However, the OSPO setup is the worst performer for these metrics on the microscale (Figure 7a, b, d and e). This is significant due to the fact that the SST and ~~2 m~~ ~~2-m~~ temperature (and resulting  $\Delta T$ ) performance for OSPO remains fairly constant from mesoscale to microscale – a finding that would suggest relative performance would also not change. The fact that a large swing in performance is found suggests that there are other larger factors in determining model performance across scales.

## 430 5 Summary and Conclusions

Utilizing a suite of mesoscale-to-microscale WRF simulations of an offshore low-level jet in which we vary the SST dataset within the model, we analyze how modeled LLJ sensitivity to SST changes across scales. This sensitivity is analyzed based on physical properties of the simulated LLJ. We find that the mesoscale domains for each SST setup generally produce too little low-level shear and under-predict the hub-height wind speed. Conversely, the LES domains over-predict both low-level shear and hub-height wind speed. The point at which the simulation shifts from ~~underpredicting to overpredicting~~ ~~under-predicting to over-predicting~~ low-level shear and hub-height wind speed is on domain 3 – the domain within the *terra incognita* or *gray zone*. We find more variation between the mesoscale domains (domains 1 and 2) for each metric than between the LES

**Table 2.** Performance ranking of each setup on the mesoscale (domain 2, specifically), gray zone (domain 3), and LES domains.

	Mesoscale Domains	Domain 3	LES Domains
Default	4	5	5
CMC	1	1	1
OSPO	2	6	7
MUR	6	3	4
NAVO	5	7	6
OSTIA	7	4	3
GOES16	3	2	2

domains (domains 4 and 5). Analyzing ensemble statistics for the jet characteristics, we find that ensemble spread in the LES domains is generally higher than the mesoscale domains and error is lower, specifically in the lower half of the rotor layer for this case. When we consider an integrated wind parameter, rotor-equivalent wind speed (REWS), we find that model performance between LES and mesoscale is more comparable. Mesoscale domain 2 REWS results are shown to out-perform LES in ensemble mean error for the majority of the period of interest.

One of the main discrepancies between the ensemble average of the mesoscale and microscale domains was in the near-surface wind speed and resulting low-level shear. The microscale domains consistently simulated weaker low-level winds resulting in being positively biased for shear below hub height while the mesoscale domains produced faster low-level winds leading to being consistently negatively biased. However, the mesoscale domains produced larger-negative sensible heat flux values during the period of interest. One would expect from this that the mesoscale domains show a higher level of stability than do the microscale domains, which would in turn produce *more* shear on the mesoscale domains. This finding leads us to believe that the mesoscale MYNN 2.5 PBL parameterization may overly mix the stable boundary layer, and/or the 1.5 order TKE sub-grid turbulence scheme on the LES domains misrepresents surface drag over the ocean. Within WRF, the surface layer parameterization calculates the surface drag coefficient based on the assumption that the near surface fluxes are fully within the sub-grid scale (SGS). When moving to LES scales, a portion of the fluxes are resolved, but the surface layer scheme underestimates the surface fluxes by only considering the SGS component in its calculation of the drag coefficient. Thus, in order to adhere to Monin-Obukhov Similarity Theory, the under-estimation of surface fluxes results in an erroneously large drag coefficient. Additionally, this may also be due in part to the fact that the current model setup neglects the wind-wave relationship such as wave state, swell-wind alignment, etc. (Sullivan et al., 2008).

Lastly, performance **Performance** is compared between setups on the mesoscale and microscale. We do this in order to answer the question of whether *we can assume that the best performing mesoscale setup will result in the best performance on the microscale?* While this analysis is subjective in how the “best” performers are determined for this single LLJ case, it represents a real-world scenario faced by many scientists in the field. For this case, the best-performing mesoscale setup, the simulation with CMC SST data, ends up being the best-performing microscale setup as well. However, the second-best-performing mesoscale setup – and one that could potentially be chosen as the best setup depending on the metric of interest – becomes the worst-performing microscale setup overall. The ranking between best and worst mesoscale performing setups is not a one-to-one match with the microscale ranking. This finding suggests that although we can try to set up our LES simulations to have the best chance of success, the differences between the mesoscale and microscale numerical methods and model setup are large

enough that one of the best performers on the mesoscale may end up being the worst performer on the microscale. Conversely, one of the worst mesoscale performers may produce the best results on the microscale. This finding is inherently tied to this case study and not necessarily general. However, for cases in which the value of SST is consistent between the finest mesoscale domain (domain 2) and the LES domains, we still see variation in performance across domains indicating that the differences between turbulence closure (PBL scheme on the mesoscale and sub-grid turbulence parameterization on the LES) is enough to cause “good” performance on the mesoscale to become “bad” performance on the LES. [These fundamental differences emphasize that studies should generally use caution when assuming that mesoscale sensitivities will directly translate to the microscale when simulating atmospheric phenomena \(such as low-level jets\) that have known dependencies on model grid spacing and turbulence closure techniques.](#)

[This study also further](#)

## 6 Discussion

One of the main discrepancies between the ensemble average of the mesoscale and microscale domains was in the near-surface wind speed and resulting low-level shear. The microscale domains consistently simulated weaker low-level winds resulting in being negatively biased for shear below hub height while the mesoscale domains produced faster low-level winds leading to being consistently positively biased. However, the mesoscale domains produced larger-negative sensible heat flux values during the period of interest. One would expect from this that the mesoscale domains show a higher level of stability than do the microscale domains, which would in turn produce *more* shear on the mesoscale domains. This finding leads us to believe that one or multiple of the following scenarios are occurring:

- The mesoscale MYNN 2.5 PBL parameterization may overly mix the stable boundary layer potentially as a result of over-predicting eddy viscosity
- Because surface turbulence stress is partially resolved, the surface layer scheme – WRF’s revised Monin-Obukhov Similarity Theory scheme (Jiménez et al., 2012) – on the LES domains misrepresents surface drag over the ocean

Within WRF, the surface layer parameterization calculates the surface drag coefficient based on the assumption that the near surface fluxes are fully within the sub-grid scale (SGS). When moving to LES scales, a portion of the fluxes are resolved, but the surface layer scheme underestimates the surface fluxes by only considering the SGS component in its calculation of the drag coefficient. Thus, in order to adhere to Monin-Obukhov Similarity Theory, the under-estimation of surface fluxes results in an erroneously large drag coefficient. Additionally, this may also be due in part to the fact that the current model setup neglects the wind–wave relationship such as wave state, swell–wind alignment, etc. (Sullivan et al., 2008).

[This study](#) elucidates the importance of further exploration into simulations within the *terra incognita*. Running weather models at these resolutions violates most currently existing turbulence closure assumptions for both the mesoscale and microscale. It has yet to be determined how best to deal with simulations at these scales whether that means skipping over

domains at this region (a large jump in parent grid ratio) or through the use of boundary layer parameterizations that are more applicable at this scale (Shin and Hong, 2015; Kosovic et al., 2016; Kosović et al., 2020). Future work will focus on the differences between mesoscale and microscale turbulence closure and surface layer parameterizations to determine the underlying differences in numerics that consistently cause slower wind speeds near the surface in the LES domains and stronger low-level shear. Additionally, similar studies for additional cases, different atmospheric phenomena, and different parametric sensitivities will be required in future studies to determine when and where mesoscale sensitivity can directly translate to microscale sensitivity.

*Code and data availability.* The NYSERDA floating lidar data were obtained through the OceanTech Services/DNV under contract to NYSERDA web portal: <https://oswbuoysny.resourcepanorama.dnv.com/>. Neither NYSERDA nor OceanTech Services/DNV have reviewed the information contained herein and the opinions in this report do not necessarily reflect those of any of these parties.

## Appendix A

The WRF Preprocessing System (WPS) is currently designed to compile with single precision. When utilizing small grid sizes,  $\Delta_x$ , the calculation of variables COSALPHA and SINALPHA, which represent the components of the rotation angle used in several map projections, are corrupted due to truncation issues when calculating the difference between latitude and longitude over a cell (See Figure A2 on Domain 2A). These variables, SINALPHA and COSALPHA, are then used within the Coriolis subroutine, gravity wave damping, and in the `pseudo-tower pseudo-tower` output (telist) when rotating the winds to Earth coordinates. Additionally, many users use these variables to rotate the model output winds to Earth coordinates in post processing. This issue has been found from the earliest version of WPS that we could obtain and, thus, will impact any simulations that consider Coriolis and/or gravity wave damping with a map projection other than Mercator. Additionally, any use of the telist output winds or postprocessing of winds to rotate to Earth coordinates will be impacted. This issue was unfortunately found in our model output after the simulation suite was conducted, thus, telist output was not used in this study and the issues associated with the COSALPHA and SINALPHA calculations are embedded in our solution.

In order to determine if precision was the issue, we calculate COSALPHA and SINALPHA offline with double precision (in our case, in Python) and then overwrite the variables in the `geo_em.d0X.nc` files. We tested this workaround by running small test cases with two domains for 48 hours with and without overwriting COSALPHA and SINALPHA to determine the impact on the wind speeds. While the calculation of COSALPHA and SINALPHA is not perfect (latitude and longitude were not calculated based on a map projection), it serves as a simple test to determine the impact of the truncation issues. The  $\Delta_x$  on these domains was set to 2500 m and 500 m, respectively. The percent difference in the wind speeds grew with time and was most significant when wind speeds were low due to small differences having a larger impact when wind speeds themselves are small (Figure A1). The differences were also larger as  $\Delta_x$  decreased in size. That said, the differences in wind speed never grew above 10% and were on average closer to 1–2% throughout the simulation on both domains. This workaround does alleviate

525 any issues in the rotation of the winds. Thus, we are confident that the basic findings of our sensitivity study are not impacted by this WRF issue. A permanent solution within WPS has been made and [will be included in the next official release](#) [have been included in WPS Version 4.5 and beyond](#).

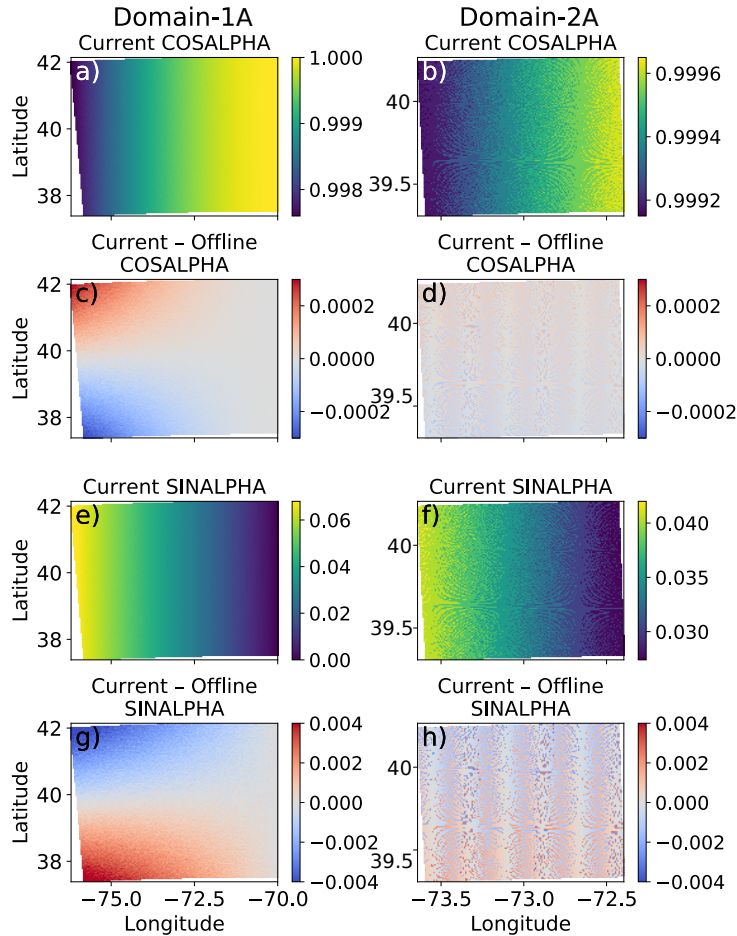


**Figure A1.** Contoured WRF-calculated COSALPHA on domains 1 and 2 (a and b, respectively), and the difference between the WRF calculation and offline calculation of COSALPHA using double precision for domains 1 and 2 (c and d, respectively). Contoured WRF-calculated SINALPHA on domains 1 and 2 (e and f, respectively), and the difference between the WRF calculation and offline calculation of SINALPHA using double precision for domains 1 and 2 (g and h, respectively).

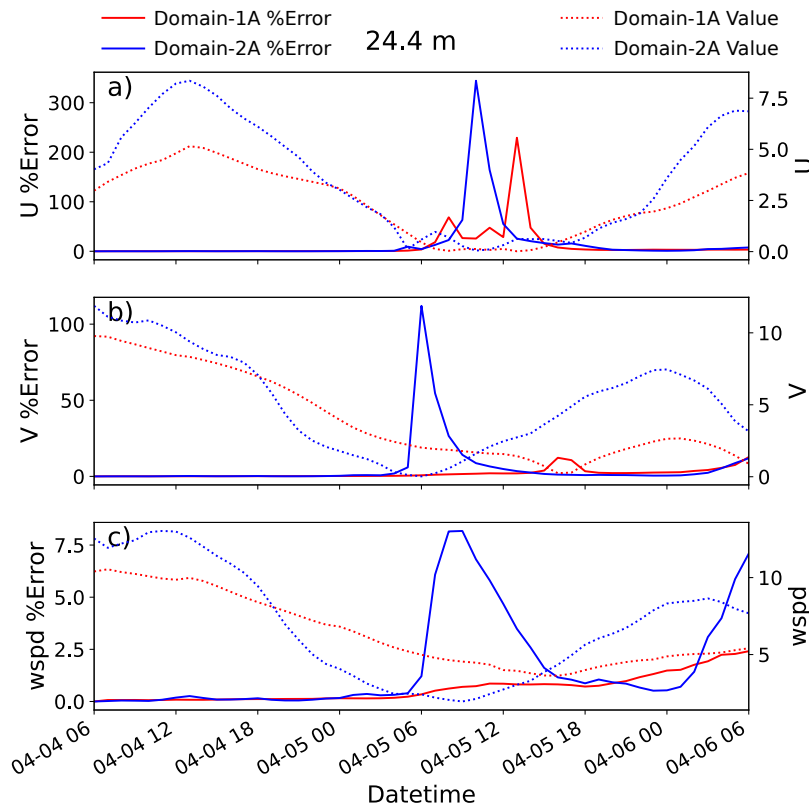


**Figure A2.** Domain-averaged percent error between the simulations with the current WRF-calculated COSALPHA and SINALPHA and the offline calculated COSALPHA and SINALPHA along with the domain-averaged value for u-component winds (a), v-component winds (b), and horizontal wind speed (c).

*Author contributions.* Conceptualization, all authors; methodology, all authors; software, PH and WL; validation, PH; formal analysis, PH; investigation, PH; data curation, PH and WL; writing—original draft preparation, PH; writing—review and editing, all authors; visualization, PH; funding acquisition, SEH. All authors have read and agreed to the published version of the manuscript.

*Competing interests.* No competing interests are present.

*Acknowledgements.* Funding Partial funding was provided by the U.S. Department of Energy Office of Energy Efficiency and Renewable Energy Wind Energy Technologies Office. The views expressed in the article do not necessarily represent the views of the DOE or the

U.S. Government. The U.S. Government retains and the publisher, by accepting the article for publication, acknowledges that the U.S.  
535 Government retains a nonexclusive, paid-up, irrevocable, worldwide license to publish or reproduce the published form of this work, or allow  
others to do so, for U.S. Government purposes. [Additional funds were provided by the Observationally driven Resource Assessment with  
CoupLEd models \(ORACLE\) project under grant number 778383, sponsored by the U. S. Dept. of Energy and managed by Pacific  
Northwest National Laboratory \(PNNL\).](#) The National Science Foundation National Center for Atmospheric Research (NSF NCAR) was  
540 a subcontractor to Pacific Northwest National Laboratory (PNNL), operated by the Battelle Memorial Institute, for the U.S. DOE under  
Contract No. DE-A06-76RLO 1830. Lawrence Livermore National Laboratory is operated by Lawrence Livermore National Security, for  
the U.S. DOE under Contract No. DE-AC52-07NA27344. NSF NCAR is a major facility sponsored by the National Science Foundation  
under Cooperative Agreement No. 1852977.

Portions of this work were performed under the auspices of the U.S. Department of Energy by Lawrence Livermore National Laboratory  
under Contract DE-AC52-07NA27344. Neither NYSERDA nor OceanTech Services/DNV have reviewed the information contained herein  
545 and the opinions in this report do not necessarily reflect those of any of these parties.

## References

- Aird, J. A., Barthelmie, R. J., Shepherd, T. J., and Pryor, S. C.: Occurrence of low-level jets over the eastern US coastal zone at heights relevant to wind energy, *Energies*, 15, 445, 2022.
- Alvera-Azcárate, A., Barth, A., Rixen, M., and Beckers, J.-M.: Reconstruction of incomplete oceanographic data sets using empirical orthogonal functions: application to the Adriatic Sea surface temperature, *Ocean Modelling*, 9, 325–346, 2005.
- Alvera-Azcárate, A., Barth, A., Beckers, J.-M., and Weisberg, R. H.: Multivariate reconstruction of missing data in sea surface temperature, chlorophyll, and wind satellite fields, *Journal of Geophysical Research: Oceans*, 112, 2007.
- Beare, R. J. and Macvean, M. K.: Resolution sensitivity and scaling of large-eddy simulations of the stable boundary layer, *Boundary-Layer Meteorology*, 112, 257–281, 2004.
- 555 Beare, R. J., Macvean, M. K., Holtslag, A. A., Cuxart, J., Esau, I., Golaz, J.-C., Jimenez, M. A., Khairoutdinov, M., Kosovic, B., Lewellen, D., et al.: An intercomparison of large-eddy simulations of the stable boundary layer, *Boundary-Layer Meteorology*, 118, 247–272, 2006.
- Beckers, J.-M. and Rixen, M.: EOF calculations and data filling from incomplete oceanographic datasets, *Journal of Atmospheric and oceanic technology*, 20, 1839–1856, 2003.
- Beckers, J.-M., Barth, A., and Alvera-Azcárate, A.: DINEOF reconstruction of clouded images including error maps—application to the  
560 Sea-Surface Temperature around Corsican Island, *Ocean Science*, 2, 183–199, 2006.
- Bhaganagar, K. and Debnath, M.: Implications of stably stratified atmospheric boundary layer turbulence on the near-wake structure of wind turbines, *Energies*, 7, 5740–5763, 2014.
- Canada Meteorological Center: GHRSSST Level 4 CMC0.1deg Global Foundation Sea Surface Temperature Analysis (GDS version 2), <https://doi.org/10.5067/GHCMC-4FM03>, 2017.
- 565 Colle, B. A. and Novak, D. R.: The New York Bight jet: climatology and dynamical evolution, *Monthly Weather Review*, 138, 2385–2404, 2010.
- Colle, B. A., Sienkiewicz, M. J., Archer, C., Veron, D., Veron, F., Kempton, W., and Mak, J. E.: Improving the Mapping and Prediction of Offshore Wind Resources (IMPOWR): Experimental overview and first results, *Bulletin of the American Meteorological Society*, 97, 1377–1390, 2016.
- 570 De Jong, E., Quon, E., and Yellapantula, S.: Mechanisms of low-level jet formation in the US Mid-Atlantic Offshore, *Journal of the Atmospheric Sciences*, 81, 31–52, 2024.
- Deardorff, J. W.: Stratocumulus-capped mixed layers derived from a three-dimensional model, *Boundary-layer meteorology*, 18, 495–527, 1980.
- Debnath, M., Doubrawa, P., Optis, M., Hawbecker, P., and Bodini, N.: Extreme wind shear events in US offshore wind energy areas and the  
575 role of induced stratification, *Wind Energy Science*, 6, 1043–1059, 2021.
- Eghdami, M., Barros, A. P., Jiménez, P. A., Juliano, T. W., and Kosovic, B.: Diagnosis of Second-Order Turbulent Properties of the Surface Layer for Three-Dimensional Flow Based on the Mellor–Yamada Model, *Monthly Weather Review*, 150, 1003–1021, 2022.
- Ferrier, B. S.: J4. 2 Modifications Of Two Convective Schemes Used In The Ncep Eta Model, in: 20th Conference on Weather Analysis and Forecasting/16th Conference on Numerical Weather Prediction, 2004.
- 580 Gadde, S. N. and Stevens, R. J.: Effect of low-level jet height on wind farm performance, *Journal of Renewable and Sustainable Energy*, 13, 013305, 2021.
- Gerber, H., Chang, S., and Holt, T.: Evolution of a marine boundary-layer jet, *Journal of the Atmospheric Sciences*, 46, 1312–1326, 1989.

- Global Modeling and Assimilation Office (GMAO): MERRA-2, const\_2d\_asm\_Nx, <https://doi.org/10.5067/ME5QX6Q5IGGU>, 2015a.
- Global Modeling and Assimilation Office (GMAO): MERRA-2, inst6\_3d\_ana\_Np, <https://doi.org/10.5067/A7S6XP56VZWS>, 2015b.
- 585 Global Modeling and Assimilation Office (GMAO): MERRA-2, const\_2d\_asm\_Nx, <https://doi.org/10.5067/IUUF4WB9FT4W>, 2015c.
- Global Modeling and Assimilation Office (GMAO): MERRA-2, tavg1\_2d\_lnd\_Nx, <https://doi.org/10.5067/RKPHT8KC1Y1T>, 2015d.
- Global Modeling and Assimilation Office (GMAO): MERRA-2, tavg1\_2d\_ocn\_Nx, <https://doi.org/10.5067/Y67YQP1L3ZZ4R>, 2015e.
- Global Modeling and Assimilation Office (GMAO): MERRA-2, tavg1\_2d\_slv\_Nx, <https://doi.org/10.5067/VJAFPLI1CSIV>, 2015f.
- Gutierrez, W., Ruiz-Columbie, A., Tutkun, M., and Castillo, L.: Impacts of the low-level jet's negative wind shear on the wind turbine, *Wind*
- 590 *energy science*, 2, 533–545, 2017.
- Hallgren, C., Aird, J. A., Ivanell, S., Körnich, H., Barthelmie, R. J., Pryor, S. C., and Sahlée, E.: Brief communication: On the definition of the low-level jet, *Wind Energy Science*, 8, 1651–1658, 2023.
- Haupt, S., Berg, L., Churchfield, M., Kosovic, B., Mirocha, J., and Shaw, W.: Mesoscale to microscale coupling for wind energy applications: Addressing the challenges, in: *Journal of Physics: Conference Series*, vol. 1452, p. 012076, IOP Publishing, 2020.
- 595 Haupt, S. E., Kosovic, B., Shaw, W., Berg, L. K., Churchfield, M., Cline, J., Draxl, C., Ennis, B., Koo, E., Kotamarthi, R., et al.: On bridging a modeling scale gap: Mesoscale to microscale coupling for wind energy, *Bulletin of the American Meteorological Society*, 100, 2533–2550, 2019.
- Haupt, S. E., Kosović, B., Berg, L. K., Kaul, C. M., Churchfield, M., Mirocha, J., Allaerts, D., Brummet, T., Davis, S., DeCastro, A., et al.: Lessons learned in coupling atmospheric models across scales for onshore and offshore wind energy, *Wind Energy Science*, 8, 1251–1275,
- 600 2023.
- Hawbecker, P., Lassman, W., Mirocha, J., Rai, R. K., Thedin, R., Churchfield, M. J., Haupt, S. E., and Kaul, C.: Offshore Sensitivities across Scales: A NYSERDA Case Study, in: *American Meteorological Society Meeting Abstracts*, vol. 102, pp. 6–2, 2022.
- Hersbach, H., Bell, B., Berrisford, P., Hirahara, S., Horányi, A., Muñoz-Sabater, J., Nicolas, J., Peubey, C., Radu, R., Schepers, D., et al.: The ERA5 global reanalysis, *Quarterly Journal of the Royal Meteorological Society*, 2020.
- 605 Holtslag, M., Bierbooms, W., and Van Bussel, G.: Estimating atmospheric stability from observations and correcting wind shear models accordingly, in: *Journal of Physics: Conference Series*, vol. 555, p. 012052, IOP Publishing, 2014.
- Iacono, M. J., Delamere, J. S., Mlawer, E. J., Shephard, M. W., Clough, S. A., and Collins, W. D.: Radiative forcing by long-lived greenhouse gases: Calculations with the AER radiative transfer models, *Journal of Geophysical Research: Atmospheres*, 113, 2008.
- Janjić, Z. I.: Nonsingular implementation of the Mellor–Yamada level 2.5 scheme in the NCEP Meso model, *NCEP office note*, 437, 61,
- 610 2002.
- Jiménez, P. A., Dudhia, J., González-Rouco, J. F., Navarro, J., Montávez, J. P., and García-Bustamante, E.: A revised scheme for the WRF surface layer formulation, *Monthly Weather Review*, 140, 898–918, 2012.
- Juliano, T. W., Kosović, B., Jiménez, P. A., Eghdami, M., Haupt, S. E., and Martilli, A.: “Gray Zone” simulations using a three-dimensional planetary boundary layer parameterization in the Weather Research and Forecasting Model, *Monthly Weather Review*, 150, 1585–1619,
- 615 2022.
- Kain, J. S.: The Kain–Fritsch convective parameterization: an update, *Journal of Applied Meteorology*, 43, 170–181, 2004.
- Kalverla, P. C., Duncan Jr, J. B., Steeneveld, G.-J., and Holtslag, A. A.: Low-level jets over the North Sea based on ERA5 and observations: together they do better, *Wind Energy Science*, 4, 193–209, 2019.
- Kosovic, B., Jiménez, P., Haupt, S., Olson, J., Bao, J., Grell, E., and Kenyon, J.: A Three-dimensional PBL Parameterization for High-
- 620 resolution Mesoscale Simulation over Heterogeneous and Complex Terrain, in: *AGU Fall Meeting Abstracts*, 2016.

- Kosović, B., Munoz, P. J., Juliano, T., Martilli, A., Eghdami, M., Barros, A., and Haupt, S.: Three-dimensional planetary boundary layer parameterization for high-resolution mesoscale simulations, in: *Journal of Physics: Conference Series*, vol. 1452, p. 012080, IOP Publishing, 2020.
- 625 Krishnamurthy, R., García Medina, G., Gaudet, B., Gustafson Jr, W. I., Kassianov, E. I., Liu, J., Newsom, R. K., Sheridan, L. M., and Mahon, A. M.: Year-long buoy-based observations of the air–sea transition zone off the US west coast, *Earth System Science Data Discussions*, 2023, 1–53, 2023.
- Liu, Y., Bourgeois, A., Warner, T., Swerdlin, S., and Hacker, J.: Implementation of observation-nudging based FDDA into WRF for supporting ATEC test operations, in: *WRF/MM5 Users’ Workshop June*, pp. 27–30, 2005.
- Liu, Y., Bourgeois, A., Warner, T., and Swerdlin, S.: An “observation-nudging”-based FDDA scheme for WRFARW for mesoscale data  
630 assimilation and forecasting, in: *Preprints, 4th Symp. on Space Weather*, San Antonio, TX, Amer. Meteor. Soc., 2007.
- McCabe, E. J. and Freedman, J. M.: Quantifying the uncertainty in the Weather Research and Forecasting Model under sea breeze and low-level jet conditions in the New York Bight: Importance to offshore wind energy, *Weather and Forecasting*, 40, 425–450, 2025.
- Mirocha, J., Kosović, B., and Kirkil, G.: Resolved turbulence characteristics in large-eddy simulations nested within mesoscale simulations using the Weather Research and Forecasting Model, *Monthly Weather Review*, 142, 806–831, 2014.
- 635 Muñoz-Esparza, D., Kosović, B., Mirocha, J., and van Beeck, J.: Bridging the transition from mesoscale to microscale turbulence in numerical weather prediction models, *Boundary-layer meteorology*, 153, 409–440, 2014.
- Muñoz-Esparza, D., Kosović, B., Van Beeck, J., and Mirocha, J.: A stochastic perturbation method to generate inflow turbulence in large-eddy simulation models: Application to neutrally stratified atmospheric boundary layers, *Physics of Fluids*, 27, 035 102, 2015.
- Musial, W., Spitsen, P., Duffy, P., Beiter, P., Shields, M., Mulas Hernando, D., Hammond, R., Marquis, M., King, J., and Sathish, S.: Offshore  
640 wind market report: 2023 edition, Tech. rep., National Renewable Energy Laboratory (NREL), Golden, CO (United States), 2023.
- NASA Jet Propulsion Laboratory: GHRSSST Level 4 K10\_SST Global 10 km Analyzed Sea Surface Temperature from Naval Oceanographic Office (NAVO) in GDS2.0, <https://doi.org/10.5067/GHK10-L4N01>, 2018.
- NASA/JPL: GHRSSST Level 4 MUR Global Foundation Sea Surface Temperature Analysis (v4.1), <https://doi.org/10.5067/GHGMR-4FJ04>, 2015.
- 645 NOAA/NESDIS/STAR: GHRSSST NOAA/STAR GOES-16 ABI L3C America Region SST. Ver. 2.70, <https://doi.org/10.5067/GHG16-3UO27>, 2019.
- Nunalee, C. G. and Basu, S.: Mesoscale modeling of coastal low-level jets: implications for offshore wind resource estimation, *Wind Energy*, 17, 1199–1216, 2014.
- OceanTech Services/DNV: <https://oswbuoysny.resourcepanorama.dnv.com/>, 2019.
- 650 OSPO: GHRSSST Level 4 OSPO Global Foundation Sea Surface Temperature Analysis (GDS version 2), <https://doi.org/10.5067/GHG16-4FO02>, 2015.
- Park, J., Basu, S., and Manuel, L.: Large-eddy simulation of stable boundary layer turbulence and estimation of associated wind turbine loads, *Wind Energy*, 17, 359–384, 2014.
- Paulsen, J., Schneemann, J., Steinfeld, G., Theuer, F., and Kühn, M.: The impact of low-level jets on the power generated by offshore wind  
655 turbines, *Wind Energy Science Discussions*, 2025, 1–37, 2025.
- Pichugina, Y., Brewer, W., Banta, R., Choukulkar, A., Clack, C., Marquis, M., McCarty, B., Weickmann, A., Sandberg, S., Marchbanks, R., et al.: Properties of the offshore low level jet and rotor layer wind shear as measured by scanning Doppler Lidar, *Wind Energy*, 20, 987–1002, 2017.

- Piety, C. A.: Radar wind profiler observations in Maryland: a preliminary climatology of the low level jet, The Maryland Department of the Environment Air and Radiation Administration Rep, 2005.
- 660 Quint, D., Lundquist, J. K., and Rosencrans, D.: Simulations suggest offshore wind farms modify low-level jets, *Wind Energy Science*, 10, 117–142, 2025.
- Redfern, S., Olson, J. B., Lundquist, J. K., and Clack, C. T.: Incorporation of the rotor-equivalent wind speed into the weather research and forecasting model’s wind farm parameterization, *Monthly Weather Review*, 147, 1029–1046, 2019.
- 665 Reen, B. P. and Stauffer, D. R.: Data assimilation strategies in the planetary boundary layer, *Boundary-layer meteorology*, 137, 237–269, 2010.
- Shin, H. H. and Hong, S.-Y.: Representation of the subgrid-scale turbulent transport in convective boundary layers at gray-zone resolutions, *Monthly Weather Review*, 143, 250–271, 2015.
- Skamarock, W. C., Klemp, J. B., Dudhia, J., Gill, D. O., Liu, Z., Berner, J., Wang, W., Powers, J. G., Duda, M. G., Barker, D. M., and Huang, X.-Y.: A description of the advanced research WRF model version 4.3, National Center for Atmospheric Research: Boulder, CO, USA, NCAR/TN-556+STR, 165, <https://doi.org/10.5065/1dfh-6p97>, 2021.
- 670 Small, R. d., deSzoetze, S. P., Xie, S., O’neill, L., Seo, H., Song, Q., Cornillon, P., Spall, M., and Minobe, S.: Air–sea interaction over ocean fronts and eddies, *Dynamics of Atmospheres and Oceans*, 45, 274–319, 2008.
- Stehly, T. and Duffy, P.: 2020 cost of wind energy review, Tech. rep., National Renewable Energy Laboratory (NREL), Golden, CO (United States), 2021.
- 675 Strobach, E., Sparling, L. C., Rabenhorst, S. D., and Demoz, B.: Impact of inland terrain on mid-atlantic offshore wind and implications for wind resource assessment: A case study, *Journal of Applied Meteorology and Climatology*, 57, 777–796, 2018.
- Sullivan, P. P., Edson, J. B., Hristov, T., and McWilliams, J. C.: Large-eddy simulations and observations of atmospheric marine boundary layers above nonequilibrium surface waves, *Journal of the Atmospheric Sciences*, 65, 1225–1245, 2008.
- 680 Sullivan, P. P., Weil, J. C., Patton, E. G., Jonker, H. J., and Mironov, D. V.: Turbulent winds and temperature fronts in large-eddy simulations of the stable atmospheric boundary layer, *Journal of the Atmospheric Sciences*, 73, 1815–1840, 2016.
- Talbot, C., Bou-Zeid, E., and Smith, J.: Nested mesoscale large-eddy simulations with WRF: Performance in real test cases, *Journal of Hydrometeorology*, 13, 1421–1441, 2012.
- Tewari, M., Chen, F., Wang, W., Dudhia, J., LeMone, M., Mitchell, K., Ek, M., Gayno, G., Wegiel, J., Cuenca, R., et al.: Implementation and verification of the unified NOAA land surface model in the WRF model, in: 20th Conference on Weather Analysis and Forecasting/16th Conference on Numerical Weather Prediction, vol. 1115, American Meteorological Society Seattle, WA, 2004.
- UKMO: GHRSSST Level 4 OSTIA Global Foundation Sea Surface Temperature Analysis, <https://doi.org/10.5067/GHOST-4FK01>, 2005.
- Wharton, S. and Lundquist, J. K.: Atmospheric stability affects wind turbine power collection, *Environmental Research Letters*, 7, 014005, 2012.
- 690 Whyte, F. S., Taylor, M. A., Stephenson, T. S., and Campbell, J. D.: Features of the Caribbean low level jet, *International Journal of Climatology: A Journal of the Royal Meteorological Society*, 28, 119–128, 2008.
- Wyngaard, J. C.: Toward numerical modeling in the “Terra Incognita”, *Journal of the atmospheric sciences*, 61, 1816–1826, 2004.
- Zhang, D.-L., Zhang, S., and Weaver, S. J.: Low-level jets over the mid-Atlantic states: Warm-season climatology and a case study, *Journal of applied meteorology and climatology*, 45, 194–209, 2006.